

9-1-1992

Applications of fourier-based features for classification of synthetic aperture radar imagery

David G. Ehrhard

Follow this and additional works at: <http://scholarworks.rit.edu/theses>

Recommended Citation

Ehrhard, David G., "Applications of fourier-based features for classification of synthetic aperture radar imagery" (1992). Thesis. Rochester Institute of Technology. Accessed from

This Thesis is brought to you for free and open access by the Thesis/Dissertation Collections at RIT Scholar Works. It has been accepted for inclusion in Theses by an authorized administrator of RIT Scholar Works. For more information, please contact ritscholarworks@rit.edu.

**APPLICATION OF
FOURIER-BASED FEATURES FOR
CLASSIFICATION OF SYNTHETIC
APERTURE RADAR IMAGERY**

by

DAVID G. EHRHARD, Captain, USAF

B.S. United States Air Force Academy

(1987)

A thesis submitted in partial fulfillment of the
requirements for the degree of Master of Science
in the Center for Imaging Science in the
College of Imaging Arts and Sciences
of the Rochester Institute of Technology

September 1992

Signature of Author: David G. Ehrhard

Accepted by: Dana G. Mareh (Coordinator, M,S, Degree Program

Date: 09-14-1992

Center for Imaging Science
Rochester Institute of Technology
Rochester, New York

CERTIFICATE OF APPROVAL

M.S. DEGREE THESIS

The M.S. Degree Thesis of David G. Ehrhard
has been examined and approved by the
thesis committee as satisfactory for the
thesis requirement for the
Master of Science degree

Dr. John R. Schott, Thesis Advisor

Dr. Roger L. Easton

Mr. Carl Salvaggio

Sept 14/92
Date

Thesis Release Permission

Rochester Institute of Technology
College of Imaging Arts and Sciences

Title of Thesis: **Application of Fourier-based Features for Classification
of Synthetic Aperture Radar Imagery**

I, David G. Ehrhard grant permission to the Wallace Memorial Library of the
Rochester Institute of Technology to reproduce this thesis in whole or in part.

Any reproduction will not be for commercial use or profit.

David G. Ehrhard

14 SEP 92

Date

**APPLICATION OF
FOURIER-BASED FEATURES FOR
CLASSIFICATION OF SYNTHETIC
APERTURE RADAR IMAGERY**

by

David G. Ehrhard

Submitted to the
Center for Imaging Science
in partial fulfillment of the requirements
for the Master of Science Degree at the
Rochester Institute of Technology

ABSTRACT

A method for segmenting synthetic aperture radar (SAR) images has been developed to operate primarily in the frequency domain. It is based on and was tested against a similar method which involves isolating information of the frequency-domain image that defines unique textural features within a class. The comparison involved classifying four simple vegetation SAR scenes with both segmentation methods. A statistical test was then performed against the null hypothesis that the new textural segmentation method is as accurate or more accurate than the original method based on random pixel classification results. All tests concluded that the texture extraction methods are not statistically different. Both methods were implemented on a mainframe computer and are computationally intensive, but the new method may be implemented optically more easily.

ACKNOWLEDGEMENTS

My research has been aided by many people whom I wish to thank. As in most accomplishments, there are many people who contributed and I am grateful because I know that without them, I could not have learned as much as I did. Specifically, I wish to thank;

Dr. John Schott, for providing the necessary guidance and vision of the "big picture" which was greatly appreciated, especially at frustrating times;

Dr. Roger Easton, for his patience and understanding in providing technical guidance in our work, especially during my strange working hours;

Carl Salvaggio, for helping get the data into a usable format, something never to be taken for granted;

Gus Braun, for helping me learn many of the tools necessary to complete my research and for BS'ing with me about everything;

Steve Schultz and Geordie Kleuber, computer system managers, for letting me be a "disk hog" at times and helping me with system problems when necessary. They have a necessary and important role and deserve my gratitude;

and Marc Comeau, my friend who helped me complete my work and keep my focus. I wish him all the best on his follow-on work.

I thank the United States Air Force for supporting me and making this all possible.

I thank my family, who have endured difficult periods of growth together. They provide me with support in everything I do. Though I seldom see them, I know that they are with me, and I with them.

Lastly, I thank God for all that I am and will be.

DEDICATION

This work is humbly dedicated to the memory of two friends who recently passed away, much too young for me to fully understand.

To *Mark Page*, whose infectious personality caused me to smile and laugh more times than I can count within the 7 months I knew him. His athletic ability, his energy for life, and his love for the people in it were unique, to say the least. He crammed 100 years into 30. Though I was only beginning to know him well and appreciate his part in my life, I am very grateful for the time we did share. His memory will live forever in my heart.

To *Miriam Epstein*, whose young innocence couldn't mask her quest for understanding life. Like Mark, she died living life to the fullest. She was very gifted yet she freely shared those gifts with her friends. While she worked too hard at times, she knew how to relax and have fun as her many friends will attest. I will miss her intense discussions (about anything important), her smile, and especially the fun we had dancing together. I wonder whether she is now dancing to Midnight Oil in heaven.

TABLE OF CONTENTS

List of Figures	x
List of Tables	xi
1.0 <u>INTRODUCTION</u>	1
2.0 <u>BACKGROUND</u>	3
2.1 Digital Imagery	3
2.2 Image Classification	4
2.3 SAR	5
2.4 Texture	9
2.5 SAR Image Classification Using Frequency-based Textural Features	13
2.6 Stromberg Method	15
2.7 Easton Method	27
3.0 <u>APPROACH</u>	31
3.1 Image Background	31
3.2 Image Preparation	31
3.3 Image Preparation With the Stromberg Method	35
3.4 Image Preparation With the Easton Method	39
3.5 Analysis of the Texture Extraction Methods	41
3.5.1 Annulus Selection	41
3.5.2 Image Classification	42
3.5.3 Classification Accuracy using Independent Polygons	42
3.5.4 Classification Accuracy using Random Pixels	43
3.5.5 Statistical Comparison	43
3.5.6 Implementation Comparison	45

4.0	<u>RESULTS</u>	46
4.1	Visual Overview of the Stromberg and Easton Methods	46
4.2	Independent Polygon Classification Results	53
4.3	Random Pixel Classification Results	56
4.4	Statistical Test Results from the Random Pixel Classification	58
4.5	Digital Implementation Comparison	60
5.0	<u>CONCLUSIONS</u>	61
6.0	<u>RECOMMENDATIONS</u>	63
	<u>REFERENCES</u>	

APPENDIX A.	FEATURES LIST
APPENDIX B.	INDEPENDENT POLYGON CLASSIFICATION RESULTS
APPENDIX C.	RANDOM PIXEL CLASSIFICATION RESULTS
APPENDIX D.	CORRELATION MATRICES
APPENDIX E.	8-8-4 SAR DATA FORMAT
APPENDIX F.	TEXTURE ANALYSIS USING EASTON'S METHOD WITHOUT CENTERING

LIST OF FIGURES

- Figure 2-1 Radar Reflection from Different Surfaces
- Figure 2-2 One-Dimensional Demonstration of Stromberg *et al.* Textural Extraction Procedure.
- Figure 2-3 Four Annuli of a Two-Dimensional Fourier Transform.
- Figure 2-4 Example of a Textural Signature Obtained from Textural Feature Bands.
- Figure 2-5 1-D Example of Stromberg's Method
- Figure 2-6 Texture Extraction using Stromberg's Method
- Figure 2-7 Texture Extraction using Easton's Method
- Figure 3-1 Image 4 (Equalized)
- Figure 3-2 Image 9 (Equalized)
- Figure 3-3 Image 28 (Equalized)
- Figure 3-4 Image 29 (Equalized)
- Figure 3-5 Illustration of Annular Ring Dimensions
- Figure 3-6 Dependence of Butterworth Lowpass Filter Magnitude on Order N.
- Figure 3-7 Example of Annulus Windows used in the Easton Method
- Figure 3-8 Example of a Centered Window of an Annulus
- Figure 4-1 Initial Steps in the Formation of an Annulus Image (from Image 9) by the Stromberg and Easton Methods
- Figure 4-2 Final Steps in the Formation of an Annulus Image (from Image 9) by the Stromberg Method
- Figure 4-3 Final Steps in the Formation of an Annulus Image (from Image 9) by the Easton Method
- Figure 4-4 Final Annulus Images Created from Image 9 using the Stromberg Method
- Figure 4-5 Final Annulus Images Created from Image 9 using the Easton Method
- Figure 4-6 Classification Maps of Image 9 Compared to Original Image 9
- Figure 4-7 Classification Maps of Image 4 Compared to Original Image 4

LIST OF TABLES

Table 3-1	Annular Ring Dimensions
Table 4-1	Summary of Independent Polygon Classification Results
Table 4-2	Summary of Random Pixel Classification Results
Table 4-3	Hypothesis Test of Proportions on Random Pixel Classification Results

1.0 INTRODUCTION

Significant research has centered on texture and its value in scene classification of visible and multispectral imagery. Less research has been accomplished in scene classification of synthetic aperture radar (SAR) imagery. Primarily as a result of technology advances in SAR and in mainframe computer capability, it is only recently that SAR imagery has been studied as extensively as have other forms of imagery.

Since the late 1970's, many studies have been conducted of scene classification of SAR imagery. Some attempted to use traditional texture-based features in the classification process while a smaller number attempted to use frequency-based features. William Stromberg and Tom Farr (1986) developed a frequency-based method in which annuli are used as bandpass filters to isolate dominant textures. After the bandpass filter, the absolute value operator and lowpass filter are used in succession to obtain an image of those frequencies. This requires two pairs of Fourier transforms; the method is effective yet cumbersome. The study that introduced this method (hereafter referred to as the Stromberg method) was primarily theoretical, however it has been used to classify both computer-generated and real SAR imagery.

Based on the work of Stromberg and Farr, Roger Easton and Jim Warnick developed a texture extraction method that also involves frequency isolation. This method (hereinafter called the Easton method) windows the transformed image to isolate the same modulating frequencies that the Stromberg method isolates. However in some cases, Easton's technique requires only one transform into and out of the frequency domain which can lead to easier implementation. Rather than compute the absolute value followed by a lowpass filter to isolate the modulating frequencies as Stromberg does, this procedure accomplishes the same thing by segmenting windows within the annulus that Stromberg

used. The window is then centered and inverse transformed where the magnitude or squared magnitude is computed. If more than one window is necessary to isolate the desired frequencies, each is processed individually and the results summed to create the segmented image. Although this procedure can be more intensive than the Stromberg procedure if many segments are used, it has potential optical implementation because it requires only linear processing, unlike the Stromberg method.

The goal of this study is to implement and compare these two algorithms using SAR imagery obtained from the Lincoln Laboratories of Massachusetts Institute of Technology (MIT). Since this research breaks new ground, the objectives are basic. Both methods for texture extraction were used to classify four simple SAR scenes containing basic textural regions. Little effort was expended to understand or eliminate image noise. The accuracy of classification was calculated in both cases based on common training areas and common independent polygons. A final random-pixel classification accuracy analysis was performed to statistically compare the effectiveness of each method for classifying the images. A statistical test of hypothesis was performed to test whether Stromberg's method is better than Easton's method. An implementation comparison is made as well as a general assessment of the optical application of the Easton method.

2.0 BACKGROUND

2.1 Digital Imagery

Throughout this work, the word *image* implies a *digital image*. Formally, a digital image can be defined as "a numerical representation of an object (which may itself be an image)" (Castleman, 1979) It is made up of a set of picture elements, called *pixels*, which are the smallest spatial unit of an image. Each pixel has an assigned *gray level* which is typically an integer in the range from zero to some maximum (e.g. 31,63, or 255) depending on the number of bits available. Zero is usually defined as black and the maximum integer is usually white. These pixels are normally arranged in rectangular raster. The original images used in this research have $512 \times 512 = 262,144$ pixels, where each is assigned a gray level in the range 0 - 255. The image can be processed for enhancement, information gathering, or classification. The *resolution* of the image is based on the distance on the ground that each pixel covers. The images used in this study have a resolution of 0.3 meters (1 foot) in both directions. For a large area to be imaged by a system with this resolution, many pixels are required. "In remote sensing the number of pixels per image is quite large, on the order of tens of millions, and consequently affects every aspect of image acquisition, processing, display and storage. Only the continuing improvements in digital electronics and computer hardware and software have made possible the routine processing of such large amounts of data." (Schowengerdt, 1983)

2.2 Image Classification

Classification is the process of separating an image into basic parts, or *classes*. Some typical classes are water, urban, forest, and grass. In this study, each pixel is assigned a class based on statistics computed as a result of supervised training. Since an image can contain a variety of classes, the classes identified within a scene are unique. The available classes in an image can also be dependent on the imaging platform, since one scanner may differentiate classes better than another. Unlike image enhancement in which the image is manipulated to be more visually acceptable for an analyst, classification separates the different classes and "assigns the decision-making process to the computer." (Schowengerdt, 1983) This can add clear advantages in speed and consistency to functions such as mapping large areas.

2.3 SAR

2.3.1 General Definition

Synthetic Aperture Radar (SAR) is an active imaging system which can produce high-resolution imagery. SAR systems are airborne or spaceborne. Like conventional radar, it is active because it must generate the energy used to produce the imagery.

2.3.2 Radar

Radar is an acronym for *radio detection and ranging*. It is a system that emits microwave energy that reflects from objects and is recorded upon its return. The strength of the return can help determine size, orientation, and material of the object. By measuring the total transmit time, the distance from the object can be calculated. Therefore, one can determine whether an object is within the field of view of the radar antenna (detection) and its precise distance (ranging). Radar systems have many uses and sizes. Some are not used for imaging, such as Doppler radar, but rather are used for determining velocities of automobiles or baseballs. Another kind is called planned position indicator radar (PPI). It is commonly used for weather and aircraft location in a large area (Lillesand,1987). The resolution of radar is determined by the size of the antenna. The larger the antenna, the better the resolution. The resolution R is governed by the relationship:

$$\boxed{R \propto \frac{\lambda}{D}} \quad (2-1)$$

Here, λ refers to the wavelength of the radar system and D refers to its antenna diameter.

2.3.3 Synthetic Aperture

Based on these radar principles, airborne and spaceborne systems would require an extremely large antenna in order to achieve high resolution. SAR systems make high resolution practical by using a *synthetic aperture*. A small radar antenna is carried on the aircraft or spacecraft that is moving at a known velocity with respect to the ground. The antenna "illuminates" a large area on the ground. As the platform moves, the radar "sees" the reflectors from different perspectives. The imaging area is to the side, typically at an azimuth of 30 degrees or more. The SAR system continually sends and receives signals as the platform moves. These continuous returns from points along the flight path are integrated to create an image. The size of the synthetic aperture is equal to the distance travelled while an object is "illuminated" by the transmitted signal. For example, an aircraft travelling at 150 miles per hour (ground speed) covers 220 feet per second. An extremely short image acquisition time of one second provides the equivalent antenna size of 220 feet. Clearly a 220 ft. antenna is unreasonable to fly on board an aircraft or a satellite. As a result, high resolutions (such as 0.3 meters in this study) can only be achieved from a SAR system.

However, a SAR system is much more complicated than traditional imaging systems. The range and azimuth data must be received and recorded continuously while the system is imaging. Then it is usually processed on a mainframe computer to generate the imagery. Because of advances in computing, the large quantity of data may be processed more easily than in the past and thus SAR images can be produced and studied more readily. However, the imagery is different than the aerial photographs we are accustomed to seeing.

2.3.4 SAR Imagery

SAR imagery is produced by deriving accurate range and angle (or azimuth) information from the microwaves that are transmitted and received. Not only does this provide for a complex system, the imagery is unique in many ways. (Toomay, 1982)

For instance:

- Since Doppler shifts are often used to measure azimuth, a moving object will be displaced from its true location on an image.
- Regardless of the angle at which the imagery is acquired, the image appears to have been "taken" directly from overhead or nearly so.
- Because of the nature of radar, SAR images can be acquired at any time of day in almost any weather.
- Brightness does not necessarily relate to a bright object as viewed by the human eye, but can be due to the material of the object or its orientation relative to the antenna.

Because electromagnetic radiation may reflect specularly or diffusely from different objects on the ground depending on material and orientation, the brightness of the object in the SAR image will vary with azimuth angle. (Lillesand and Kiefer, 1987) A stronger return will generate a brighter area on an image. Figure 2-1 shows the influence of different types of reflectors on the image. Because orientation of the object relative to the antenna is important, a low grazing angle may yield very little return from a diffuse reflector, while a high grazing angle to a spectral reflector may return a very high signal.

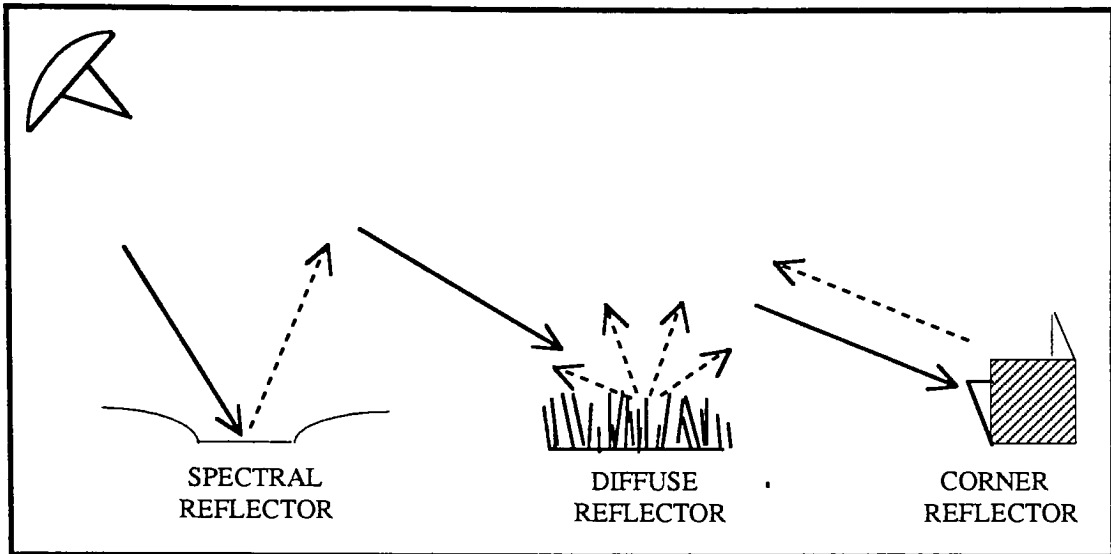


Figure 2-1 Radar Reflection from Different Surfaces

Lillesand and Kiefer (1987) state that high returns can result from objects with slopes facing the antenna, objects with high moisture content, metal objects, or urban areas with buildings that resemble corner reflectors. Variation in texture in an area will often resemble the diffuse reflector. Little or no return is received from flat areas such as calm water or pavement.

2.3.5 Polarization

SAR imagery are also affected by the polarization of the transmitted and received modulation. Polarization refers to the orientation of the waves as they are sent and received by the radar antenna. Typically the signals are oriented either horizontally (H) or vertically (V). As a result, there are four possible send/receive combinations; HH, HV, VH, and VV, where the letters refer to wave orientation when transmitted and received, respectively. Different orientations will reflect radar signals better from different objects (Lillesand and Kiefer, 1987). Since this research uses an equal combination of all polarizations, an explanation of the distinctive properties is unnecessary.

2.4 TEXTURE

2.4.1 General Definition

The Random House College Dictionary defines *texture* as "the characteristic physical structure given to a material by the size, shape, density, arrangement, and proportions of its elementary parts." (Stein, 1980) In image processing circles, texture is defined as "some local property of an image, *i.e.* a measure of the relationship between the pixels in a neighborhood." (Schowengerdt, 1983) It is this definition of texture that is commonly used in image classification.

Haralick *et al.*(1973) refers to three basic features of color or multispectral imagery: spectral, textural, and contextual. Spectral features are the tonal variations between different spectral bands of an image. Spectral features have been successfully used with textural features for image classification in many studies. However, because this study uses only SAR imagery at one wavelength, spectral features are not relevant. Contextual features are based on the surroundings of the area under study. One example of a contextual feature in an aerial image is that a school is usually surrounded by grass and usually has a playing field contained within a running track near bleachers. These features are usually large (covering many pixels in an image), however, and they are often difficult to quantify for computer analysis. The textural features of an image contain information about spectral tone variation and spatial arrangement which can be quantified and have been widely studied for image classification. Haralick *et al.* (1973) refers to texture as being "extremely refractory to precise definition and to analysis by digital computers." Textures therefore can contain useful information to discriminate between different areas of an image.

2.4.2 Texture Characterization

In her study of classification using textural features, Rosenblum (1990) reviews the common ways to characterize texture. The study actually used four methods:

1. Co-occurrence statistics - These count the number of equally valued pixels that are located in specific orientations from one another in a quantized image. The number of different co-occurrence features depends on window size.
2. First-order statistics - The texture is described by the mean(μ) and standard deviation (σ) of the brightness values within the window of the measurement.
3. Run-length statistics - This is the measure of the number of pixels of a given gray level that are oriented in a certain direction. For example, when analyzing a corn field one would find more of the same brightness levels along the direction of the rows than across the rows.
4. Edginess measure - This is a filter which detects differences in brightness. A Roberts gradient or any derivative operator will perform this function. A window containing a consistent smooth texture such as water would yield little or no gray value while an urban area or rough texture would result in a large number.

The four categories of texture characterizations account for 46 of the 49 features used in the feature optimization software that Rosenblum helped develop. A list of all 49 can be found in Appendix A. The last three are spectral bands which do not apply to the SAR imagery.

2.4.3 Image Classification Using Textural Features

Haralick *et al.*(1973) used textural features to classify three different kinds of imagery. He achieved classification accuracy of 89% in photomicrographs of different sandstone categories, 82% in aerial photographs, and 83% in satellite imagery. While he used spectral bands to classify images where applicable, he found that the highest accuracy was obtained by including the textural features. Specifically, the angular second moment, the entropy, the sum entropy, the difference entropy, the information measure of correlation, and the maximal-correlation features proved to be the most suitable for further study.

Haralick's study was among the first of many that used texture to better classify imagery by computerized methods. Later in the 1970's and 1980's, SAR imagery was increasingly used to study the value of textural features in classification. For example, Ulaby *et al.* (1986) studied texture in SAR images by using first-order and second-order statistics as features to classify rural Seasat and SIR-A (Shuttle Imaging Radar) SAR images. Maximum likelihood classification was used for five classes: water, forest, pasture, urban, and cultivated. Up to 72% accuracy was obtained with the first-order statistics and 88% with the second-order statistics on the Seasat images. The accuracy went up to 75% and 93% when applying the same techniques to forested regions with five classes of forest types. The resolutions of the images in Ulaby's study varied and image noise was treated as statistically independent of the textural variations of the target classes.

Frequency-based features began to emerge as an addition to traditional textural features in the 1980's. Different textures often have different frequency-space characteristics. As a result, different textures are distinguishable and can be used for image classification. As in this study, the Fast Fourier transform (FFT) is often used to convert

an image from the spatial domain to the frequency domain. Summaries of past research efforts in this area are presented in the next section. These studies provide much of the background for this work which evaluates two of the newer frequency-based feature extraction methods.

2.5 CLASSIFICATION OF SAR IMAGES USING FREQUENCY-BASED TEXTURAL FEATURES

Many groups studied texture in synthetic aperture radar (SAR) imagery as it became more available. Some problems exist due to the difference in interpreting SAR imagery relative to visible images, the large amount of image noise often existing in the images, and the lack of images because there are few collection systems. Most work with SAR imagery has been carried out in the last decade.

Burl *et al.* (1989) studied texture discrimination of high-resolution SAR imagery (0.3m x 0.3m) to distinguish between man-made objects and ground clutter. The three features used include: fractal dimension, log standard deviation, and ranked fill ratio. These features were found to "show promise" for the intended discrimination. Only the HH polarization was used and it was manipulated to the single-polarimetric-channel $|HH|^2$, the squared modulus. Nothing was done to reduce image noise and while the results of the feature calculations were tabulated, the discrimination was subjective.

Burns and Lyzenga (1984) found that texture was useful for classifying sea ice imagery. They did not correct for speckle noise and yet found a variety of textural features to be valuable for classifying SAR images. These include: digital Fourier transforms, spatial gray-level co-occurrence probabilities, statistics of local properties, and autoregressive models. The authors were optimistic about using these features for scene classification, however no quantitative results were reported nor were the features compared. They stated that "little work has been done to determine the optimum technique for a given application."

Holecz *et al.* applied four different textural features to SAR images of terrestrial regions. Although this study involved geocoding the images and speckle investigation, the

images were classified with and without manipulation. The four textural features applied are: the Spatial Gray Level Dependence Method (SGLDM), the Gray Level Run-Length Method (GLRLM), the Gray Level Difference Method (GLDM), and the power spectrum method (PSM). Of interest here are the results comparing PSM, a frequency-based feature similar to a Fourier transform, and the three spatial domain features. This study showed the dominance of SGLDM in classifying the images of countryside in Switzerland. PSM ranked lowest because the window size used was 7×7 , the writers postulated. They suggested the window should be larger when using the digital Fourier transform (DFT) thinking that a larger window size would provide more useful information.

All of these methods classified SAR images with some success. Few new approaches were taken that have not been attempted on other types of imagery. However, a body of knowledge was built which allows others to better understand and classify SAR imagery and potentially other types as well. In addition to these studies, one other promising technique that has not been rigorously tested on actual SAR imagery is explained in the next section.

2.6 STROMBERG METHOD

William Stromberg and Tom Farr (1986) proposed a procedure for extracting textural features which they applied to SAR images. For ease of reference, it has been called the Stromberg method. The method filters the Fourier transform with annular rings to isolate frequencies that correspond to a given texture within an image. That texture can be used to distinguish from other classes which have different textures. This method was validated by using different synthetic images and SIR-A images of Belize (Central America), a tropical and heavily vegetated area.

Stromberg's method of classification involves isolating a modulation function which will be used to characterize the texture of interest. The modulation function is the dominant texture (or frequencies) in the class of interest. One assumption is that different classes of an image contain different textures and therefore contain different frequency characteristics (modulation functions). To isolate the modulation function of a texture, Stromberg proposes a method with eight steps performed in succession. They are:

1. Compute the Fourier transform of the image,
2. bandpass filter the result using an annulus in the frequency domain,
3. compute the inverse Fourier transform,
4. compute the absolute value,
5. Compute the Fourier transform,
6. lowpass filter the result,
7. compute the inverse Fourier transform (frequency to spatial domain)
8. Apply a box filter to the result. (averaging operation used to eliminate noise and rough edges)

This procedure will isolate a unique modulation function and its neighboring frequencies for the window of interest. These isolated functions are processed and the resulting frequency band images are then used together to separate the textures in the

classification process because each texture contains unique contributions from each of the frequency band images. Stromberg's examples will be used to explain the steps, first in one dimension.

First, $c_0(x)$ is the space-domain representation of a "key" Fourier component of the texture at frequency ω_0 with period $T_0 = 2\pi/\omega_0$. Since Fourier components are complex valued, $c_0(x)$ is defined as an equivalent real-valued function generated from the sum of two Fourier components at equal positive and negative frequencies. In this example, $c_0(x) = \cos(\omega_0 x)$. Subsequently, the Fourier transform, of this cosine is the sum of delta functions at $\pm \omega_0$.

$$C_0(\omega) = \frac{1}{2} [\delta(\omega - \omega_0) + \delta(\omega + \omega_0)] \quad (2-2)$$

Since it is the key component of the Fourier transform, its amplitude varies throughout the image via the modulation function $m(x)$. This is the function isolated in the procedure.

$$d(x) = m(x) c_0(x) = m(x) \cos(\omega_0 x) \quad (2-3)$$

Multiplication in the spatial domain is equivalent to convolution in the frequency domain. As a result, the Fourier transform of $d(x)$, $D(\omega)$, is in the equation 2-4, where $M(\omega)$ denotes the Fourier transform of the modulation function $m(x)$ and "*" denotes convolution.

$$D(\omega) = M(\omega) * \frac{1}{2} [\delta(\omega - \omega_0) + \delta(\omega + \omega_0)] \quad (2-4)$$

From the sifting property of a delta function under convolution, $D(\omega)$ consists of $M(\omega)$ replicated at $\pm \omega_0$. Figure 2-2(c) and (d) shows an example of $d(x)$ and $D(\omega)$.

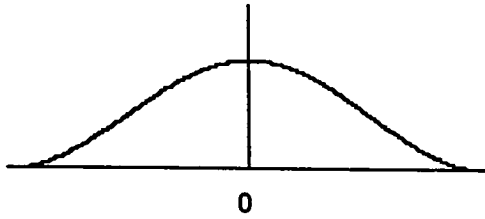
$$\boxed{D(\omega) = M(\omega - \omega_0) + M(\omega + \omega_0)} \quad (2-5)$$

Once again, the goal of this method is to isolate the modulation function $m(x)$ which will be used to distinguish textures. Stromberg separates $m(x)$ from $d(x)$ by first computing the inverse Fourier transform. He then computes the absolute value of $d(x)$ in the space domain and lowpass filters the result in the frequency domain. Computation of the absolute value of $d(x)$ replicates the modulation transform $M(\omega)$ at odd multiples of ω_0 . To extract $m(x)$, only the component at the origin of the frequency domain need be isolated. This is accomplished by an ideal lowpass filter which passes all information at $\omega \leq |\omega_0|$ and rejects all else. Figure 2-2 shows the one-dimensional method that Stromberg uses to base his method of texture extraction for SAR image classification.

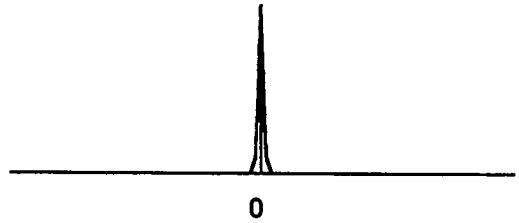
Figure 2-2(a) shows a raised cosine wave which might be a modulation function. Figure 2-2(b) shows the Fourier transform of (a), a delta function at the origin. Figure 2-2(c) shows a cosine wave multiplied by (or modulated by) the modulation function of Fig. 2-2(a). Like the equation above, the higher-frequency cosine takes the form of $c_0(x) = \cos(\omega_0 x)$. In the Figure 2-2, "w" is the same as " ω_0 ". Figure 2-2(d) is $D(\omega)$, the Fourier transform of $d(x) = m(x) c_0(x) = m(x)\cos(\omega_0 x)$. This function would be bandpass filtered to isolate desired modulations in step 2 (above). In this idealized case, the one-dimensional bandpass filter operates is a pair of rectangle functions, while the corresponding function in two dimensions is an annulus. To isolate the modulation function, Stromberg applies the absolute value operator to the function of Figure 2-2(c) which results in Figure 2-2(e). The Fourier transform of Figure 2-2(e) yields Figure 2-2(f) which shows in the one-

dimensional case the modulation function replicated at odd multiples of ω_0 . This can be filtered to isolate only the central region of the result by lowpass filtering (step 6) to get Figure 2-2(g), still in the frequency domain. It is transformed back to the space domain via the inverse Fourier transform and a function which resembles the original modulation function is the result, Figure 2-2(h).

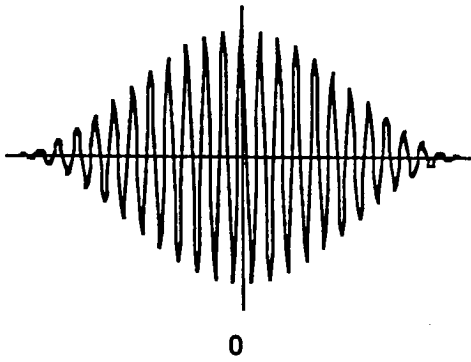
The theory is then extended to two dimensions and eventually to real imagery. To do so, some assumptions are made. Unlike the example shown above, texture is seldom characterized by discrete non-overlapping peaks in the frequency domain. Therefore, the assumption is made that the effect of one frequency component on another decreases as the separation between the two increases. Additionally, the effect of one textural component on another becomes insignificant beyond a narrow range of spatial frequency. Based on experience, Stromberg defines the "narrow range" as 6% of the Nyquist frequency. He uses the central peak of a sinc function as a weighting function to separate potential modulation functions.



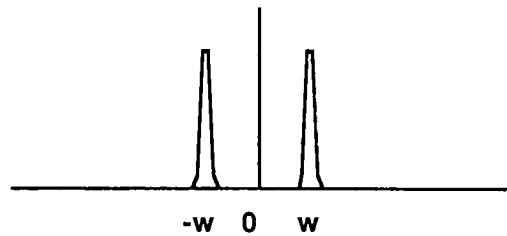
(a) Modulation function $m(x)$ to be isolated



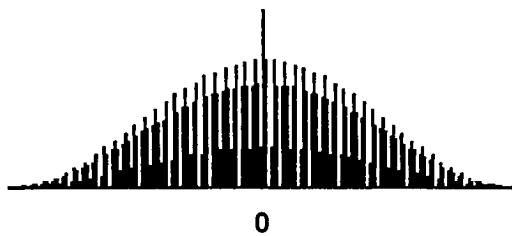
(b) Frequency domain $M(\xi)$



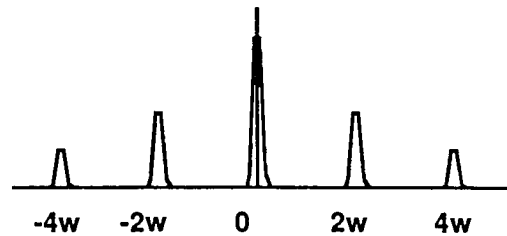
(c) $d(x) = m(x) \cos(\omega x)$



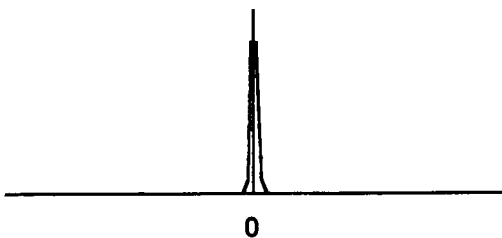
(d) $D(\omega)$



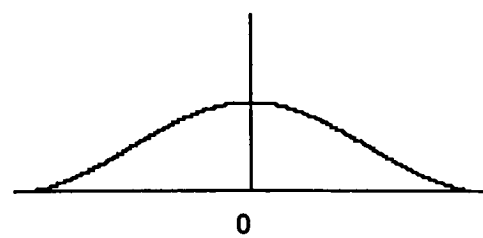
(e) $|d(x)|$



(f) $F(|d(x)|)$



(g) Lowpass Filter of (f) above



(h) Reproduction of $m(x)$ from
inverse FFT of (g)

Figure 2-2 One dimensional demonstration of Stromberg *et al.* (1986) textural feature extraction procedure.

Directional dependence is also a consideration. In one dimension, a sinusoid reacts differently than in two dimensions. A textural feature image formed from a Fourier texture metric will not respond identically when the space-domain image is rotated as compared to the result if it is not rotated because the frequency-domain changes as well. The two-dimensional Fourier transform result is rotated if a textural orientation is rotated in the space domain. This can result from an airborne platform simply flying a different heading over the same land. Since imagery may have all variations of directionality with respect to land textures, directional independence is desirable for an image classification procedure. As a result, Stromberg introduces the textural component that lies in a ring centered at the origin of the Fourier transform, commonly called an annulus. Eventually, he applies more than one annulus to a Fourier representation depending on the number of textural components that exist. Figure 2-3 illustrates an example which has 4 annuli.

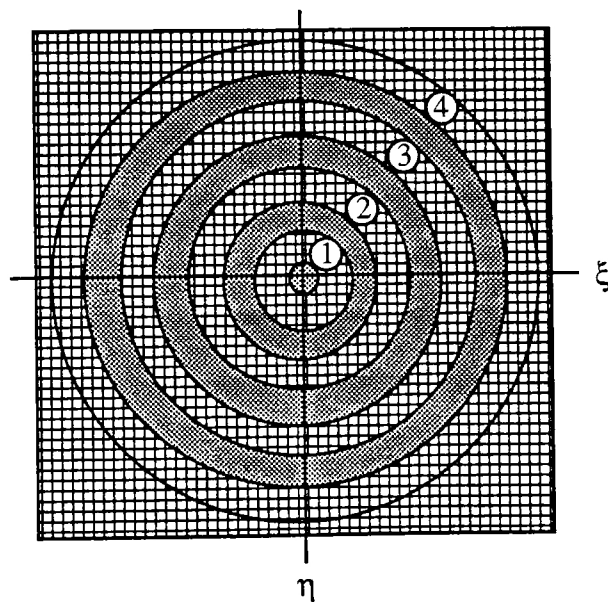


Figure 2-3 Four Annuli of a Two-Dimensional Fourier Transform.

Stromberg then applied his method to synthetic imagery. This was performed to verify three assumptions:

- 1) a two-dimensional key component bears the appearance of a single frequency;
- 2) the modulation of a key component is predictable, exhibiting variation which corresponds to the relative contribution of the key component to the local texture;
- 3) the modulation function is recoverable through absolute value and lowpass filtering operations.

Each annulus used to bandpass filter the image produces its own feature image. Together, these textural feature images are used to classify the original image. In addition, two other products are used: a classification map and a set of textural signatures.

These two products are cited as examples of uses for textural features. The classification map is a means to qualitatively discriminate regions of unique texture by viewing each of the images in the process. The original image, the intermediate filter band images, and resultant classification images are all displayed in order to visually inspect the process and the results. The textural signatures can be used to quantitatively assess each textural class. Figure 2-4 is an example of a signature from one of the textures Stromberg tested.

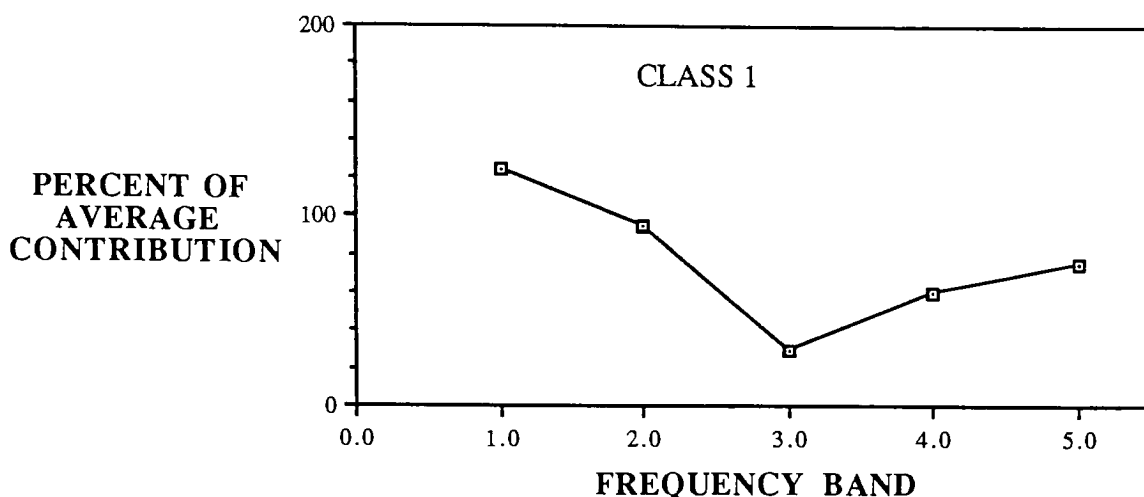


Figure 2-4 Example of a textural signature obtained from textural feature bands.

A class is described by a signature which is derived from the mean value of each textural feature band (corresponding to a single annulus) as a percentage of the average contribution over all classes. Each textural signature represents the unique set of contributions from the entire set of pass bands to that class. Figure 2-4 shows an example of five bands contributing to one class. Another class will yield different contributions from the same five bands, and still another class will yield a third combination. Stromberg computes the percentage (on the Y-axis) such that one band averages 100% over all of the classes. In addition, all five bands may not average 100% for one class as is the case in Figure 2-4 and is the case for most classes. For example, one class may have a very low contribution from all of the bands while another may have very high contributions from all five bands. Each combination of contributions is unique.

Because of the practical results of the Fourier transform, an adaptive normalization was used to maintain dynamic range. Stromberg needed to boost the high-frequency bands so that those contributions could compare to the more powerful low-frequency bands.

To discriminate between regions of uniform texture, Stromberg uses a general purpose unsupervised clustering algorithm designed for some other applications not specified. Class statistics are computed for each image sample of a given class using first-order and second-order statistics. The Euclidean distance of each N-dimensional image sample from the existing texture is compared to a threshold distance d . If the distance is smaller than d to any texture class, the sample is assigned to that class. If not within a distance d of a cluster, it is assigned as a new cluster. Stromberg adjusted d until only five classes remained after performing this technique. Then he passed the statistics to a Bayes classifier for image sample classification.

When applied to synthetic imagery, Stromberg achieved 97.6% classification accuracy with this method. The 2.4% of samples which were misclassified appear on the borders between classes.

Stromberg then generated synthetic imagery modelled from transforms of geologic imagery. He added Gaussian noise from a random noise generator in the frequency domain which had the effect of adding artificial texture to the imagery in the spatial domain. The annuli used for this imagery had the same mean frequency, but half the width. He used an unsupervised classifier and increasing the threshold distance d until five classes were distinguishable. The same Bayes classifier was used to discriminate at the pixel level. As expected, the classification accuracy decreased to 89.9%. The errors were primarily in the fifth class which corresponds to the highest frequencies. As before, the majority of the errors were near class boundaries.

In its final test, Stromberg applied the method to real SAR imagery. The images were obtained from the Shuttle Imaging Radar-A (SIR-A). The area was a heavily vegetated region of Belize, a Central American country on the Caribbean Sea which borders Mexico and Guatemala. The images were used to investigate the slope and topographic

information of SAR imagery of a jungle area. Here, the slope and topography are used as the texture to be discriminated in Stromberg's classification method. No quantitative results were given for this test. However, it is noted that the classification image bears "close resemblance" to the actual geologic map of the area.

Figure 2-5 shows another example of the Stromberg Method in one dimension. Unlike the first example in Figure 2-2, this example shows the different frequencies overlapping in the frequency domain representation (b). The isolated square wave is in the center of the other two (a). Some of the same characteristics exist in this example as in the first. The process finally locates the position of the original selected square wave, but it is not precise. In this case, the "blurry" affect is a result of using a very narrow bandpass filter $H[\xi]$ in (c). If one uses a wider filter, the location in the output (g) will be more pronounced, or less "blurred".

Figure 2-6 shows the result of Stromberg's method when applied to a 64 x 64 synthetic image. Note that a frequency may be present in more than one quadrant of the image. In this case, the annulus isolates the frequencies that are present in three of the quadrants (none is present in the lower right quadrant). The output image was obtained from a single annulus and could be used as one input into the ERDAS classification routine along with other annulus images and the original magnitude image.

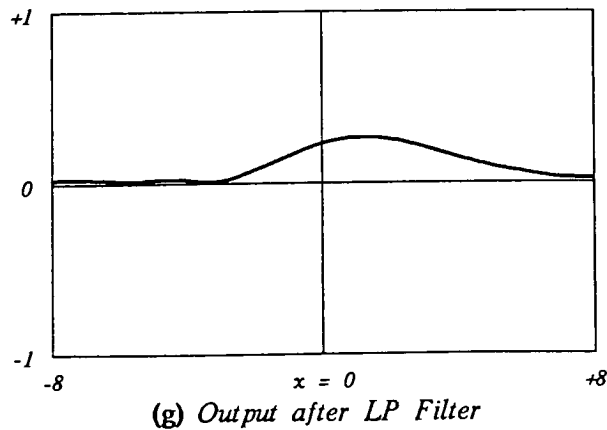
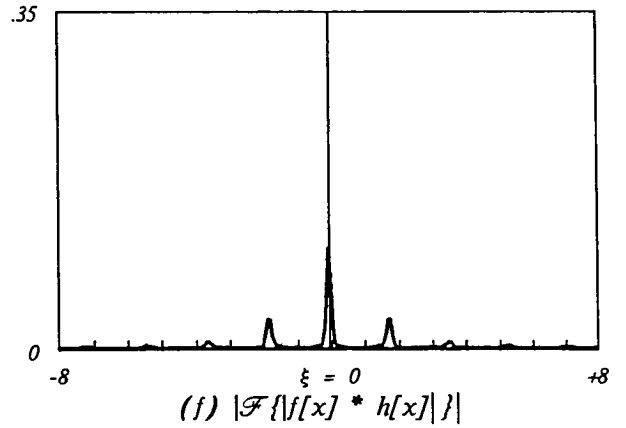
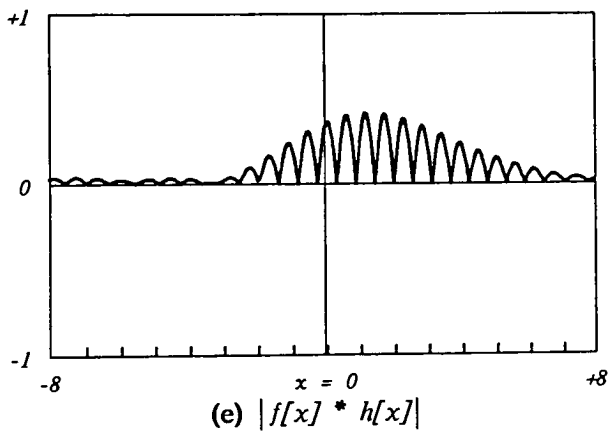
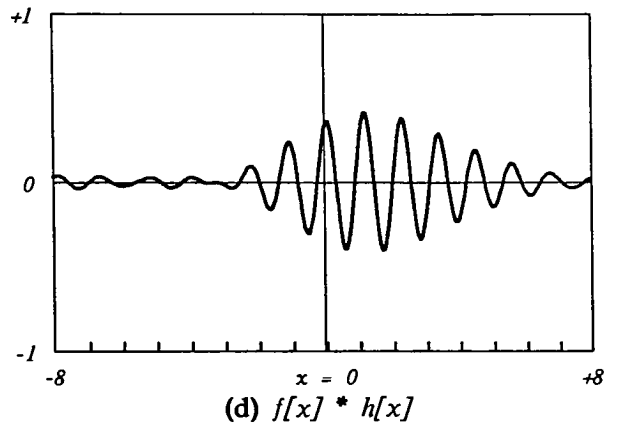
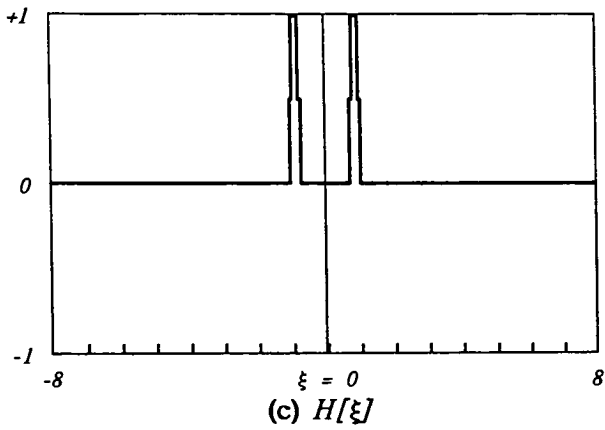
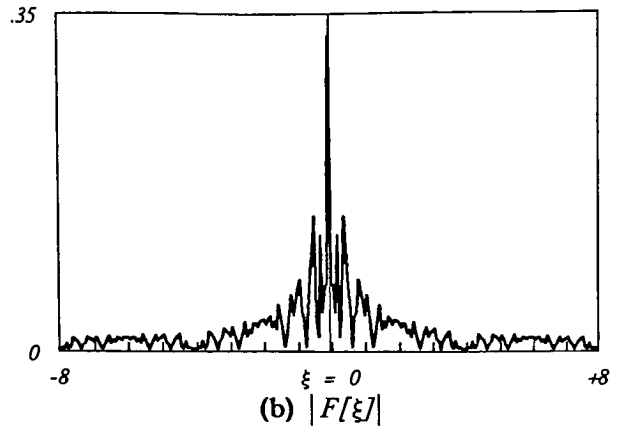
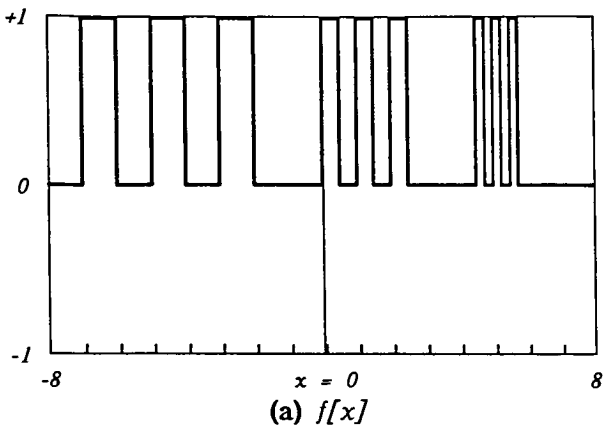
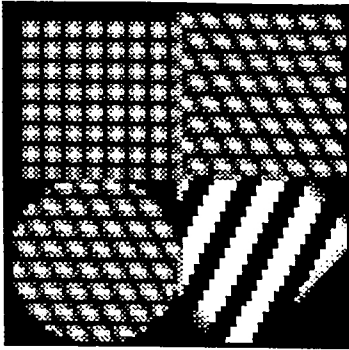
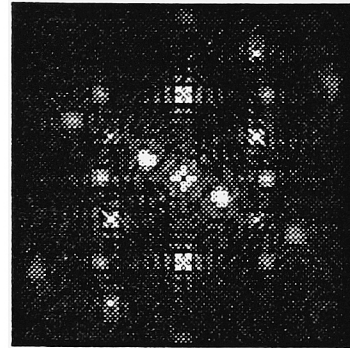


Figure 2-5: 1-D Example of Stromberg's Method
25

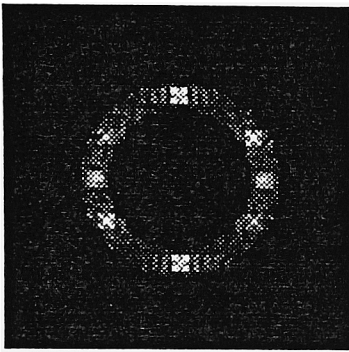
(a) $f[x,y]$



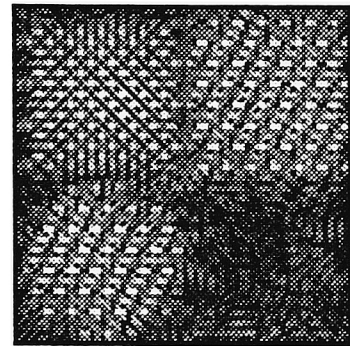
(b) $|F[\xi,\eta]|$



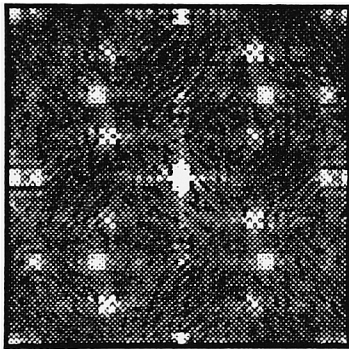
(c) $|F[\xi,\eta] \cdot A_1[\xi,\eta]|$



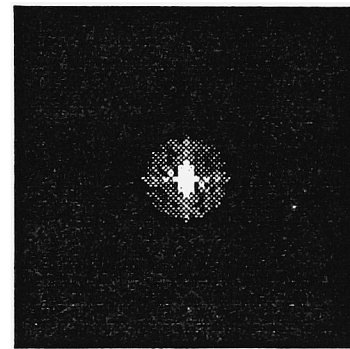
(d) $|f[x,y] * a_1[x,y]|$



(e) $\mathcal{F}\{|f[x,y] * a_1[x,y]|\}$



(f) $A_2[\xi,\eta] \cdot \mathcal{F}\{|f[x,y] * a_1[x,y]|\}$



(g) $|\mathcal{F}^{-1}\{A_2[\xi,\eta] \cdot \mathcal{F}\{|f[x,y] * a_1[x,y]|\}\}|$

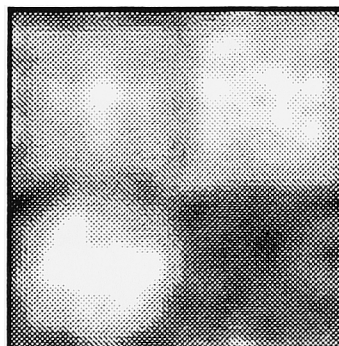


Figure 2-6 TEXTURE ANALYSIS USING STROMBERG'S METHOD

2.7 EASTON METHOD

Although the Stromberg method has been tested on synthetic images and on real SAR images on a limited basis, it is computationally intensive. Four Fourier transforms must be computed to isolate the modulation function that is used to find a texture within the image. An effort was made to simplify the Stromberg method and decrease the number of computations.

Dr. Roger Easton has created a method for feature extraction in the frequency domain that is similar to the Stromberg method. For ease of reference this has been called the Easton method. The main difference between the two methods is that the Easton method requires fewer Fourier transforms and it avoids the nonlinear absolute value operator.

To review, the Stromberg method isolates a frequency component by using the bandpass filter, the absolute value operator, and the lowpass filter to isolate unique modulating frequencies that will distinguish one textural region from others. More specifically, the Stromberg method involves applying an annulus (2) to bandpass filter the Fourier transformed image (1). It is inverse transformed (3) and the absolute value operator (4) is applied so that the modulation function can be more easily isolated by lowpass filtering (6) the transformed (5) image. The inverse transform (7) shows the area of the original image where the isolated frequency existed. This is the desired result for image classification. The box filter (8) is applied to remove some of the undesirable noise that remains through the entire process.

The Easton method does not require the second and third Fourier transforms (steps 3 and 5) because it isolates the modulation function differently in the frequency domain after the first Fourier transform. Instead of applying a complete annulus, a window is used

to isolate frequencies that lie within the annulus. A number of windows may be used within a given annulus, depending on the dominant frequencies identified. The effect of Stromberg's absolute value and lowpass filter is accomplished by translating windows of the annulus to the center of the image and inverse transforming, one by one. The magnitudes of the outputs for each window are summed after each frequency window is inverse transformed. The magnitude is computed separately from other windows so that phase information is not cancelled during the summation. In this manner, the positional information is preserved which locates the isolated frequencies in the spatial domain. The summation of these images produced from windowed frequencies is very similar to the annulus image created in step 7 of Stromberg's method.

The total area of the windows will not exceed and often will be much less than the total annular area since useless areas are not added. It is expected that some parts of a given annulus are more useful than others for achieving the desired classification results. This can be determined based on the gray levels within the annulus and is not investigated in this study. Each window of a given annulus should be roughly the same size, depending on the frequencies isolated. Higher-frequency annuli will require larger windows because a larger area is needed to isolate a given frequency return at higher frequencies. The total number of steps for this new texture extraction method is determined by the number of windows chosen since each is treated individually. The Easton method does not require the use of annuli to distinguish or to isolate strong frequency returns. However, since it is essential to this study for comparison to the Stromberg method, it is incorporated in the original theory. The steps for the Easton method are:

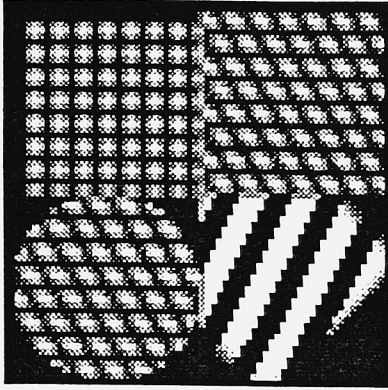
1. Compute the Fourier transform of an image,
2. isolate a window at a location in the frequency domain with a bright return,
3. translate the window to the center of the frequency domain,
4. compute the inverse Fourier transform,
5. calculate the magnitude of the resulting space-domain image,
6. add to other space-domain images derived from that annular region.
7. Choose another window if necessary. (go to step 2)
8. Box filter the resulting annular image if necessary.

The Easton method has been tested on synthetic images. Figure 2-6 shows an example. The box filter was not applied since it is more applicable to noisy images. This illustrates the simplest result of a single window used to isolate one frequency. Notice that a window is isolated and then is used as the center of the new frequency image.

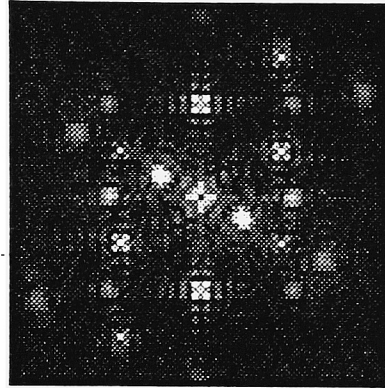
Unless the entire annulus is windowed, this method does not offer the directional independence that is a characteristic of the Stromberg method. However, effective window selection could overcome that shortfall if the imagery has some directional dependence.

Both the Easton method and the Stromberg method were tested on SAR imagery by comparing classification results. Both methods were modified slightly in order to facilitate implementation and to keep the comparison fair.

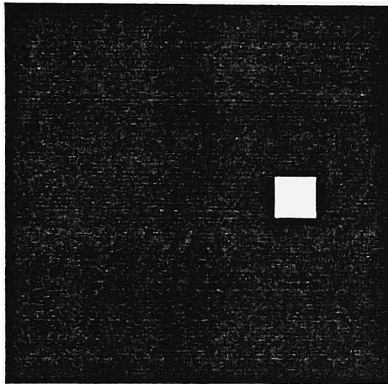
(a) $f[x,y]$



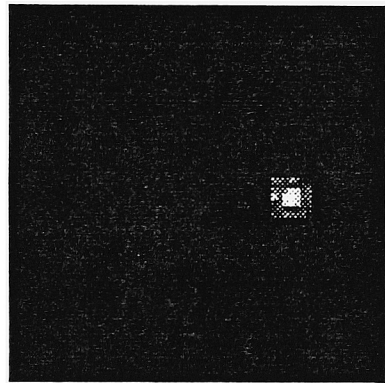
(b) $|F[\xi,\eta]|$



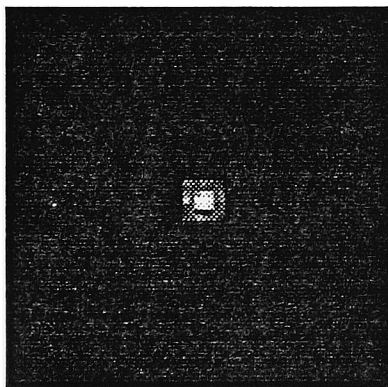
(c) $A_1[\xi,\eta]$



(d) $|F[\xi,\eta] \cdot A_1[\xi,\eta]|$



(e) $F[\xi,\eta] \cdot A_1[\xi,\eta] * \delta[\xi-\xi_0,\eta]$



(f) $\mathcal{F}^{-1}\{F[\xi-\xi_0,\eta] \cdot A_1[\xi-\xi_0,\eta]\}$

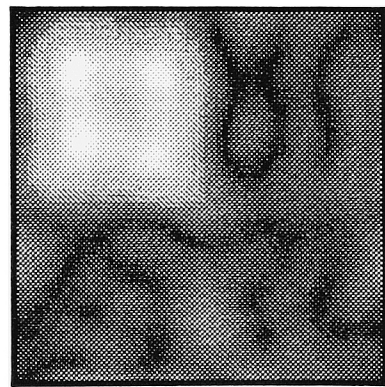


Figure 2-7 TEXTURE ANALYSIS USING EASTON'S METHOD

3.0 APPROACH

3.1 Image Background

The SAR images were obtained by RIT's DIRS laboratory from MIT's Lincoln Labs. The imaging platform was developed under a Defense Advanced Research Projects Agency (DARPA) sponsored Advanced Detection Technology (ADT) program. ADT uses a high resolution (0.3m by 0.3m), fully polarimetric, synthetic aperture radar (SAR) that operates at a center frequency of 33.56 GHz. It was built by Loral Systems and was flown in a Gulfstream G-1 aircraft for acquisition of the images used in this study. The images were acquired on the morning of 25 May 1989 over Stockbridge, New York.

3.2 Image Preparation

Once the SAR image data was copied to VAX disc, each image was converted from its compressed 884 format (explained in Appendix E) to complex format. Each scene consists of four polarizations: HH, HV, VH, and VV. An image was created for each one by computing the magnitude of the complex data at each pixel. The equation for the HH polarization follows where i and j are row and column values:

$$\text{Mag}(\text{HH})_{ij} = \sqrt{\text{REAL}(\text{HH})_{ij}^2 + \text{IMAGINARY}(\text{HH})_{ij}^2} \quad (3-1)$$

The different polarizations for each image were then combined to form a single 512 x 2048 image. In this case, the magnitude images were combined by using the geometric mean in order to minimize noise as simply as possible. The equation follows:

$$\text{Mag}_{ij} = \frac{\sqrt{\text{Mag}(\text{HH})_{ij}^2 + \text{Mag}(\text{HV})_{ij}^2 + \text{Mag}(\text{VH})_{ij}^2 + \text{Mag}(\text{VV})_{ij}^2}}{4} \quad (3-2)$$

The images were then converted to 8-bit digital data for display and ease of computer time and space.

The 512 x 512 images were extracted from these 512 x 2048 images by visually inspecting the equalized image to find a region of sufficient clarity and definition. Since the objective of this research involves performing initial classification tests on these SAR images, the clearest areas of simple context were chosen. The images contain classes of grassy areas, forested areas, shadows from the trees, and some small roads.

The images chosen for this study will be referenced based on the nomenclature used by Lincoln Labs. Of 16 scenes, four are from Mission 85 Pass 5 (Frames 27, 28, 29, and 30) and twelve are from Mission 90 Pass 5 (Frames 0 - 11). For ease of reference, the names of all images are based on the frame numbers listed above. Unless otherwise stated, the name also refers to the 512 x 512 image cut from the original 512 x 2048 image. The four selected are images 4, 9, 28, and 29. The equalized images are shown in Figures 3-1 to 3-4. The images (after equalizing the histograms) are shown because they are more visually pleasing than the original combined magnitude images.

Images 4 and 28 were chosen because they are the most basic. Each has three obvious classes to distinguish: grass, trees, and shadows. Images 9 and 29 also contain roads along with the other three classes in order to further test the robustness of the Stromberg and Easton methods.

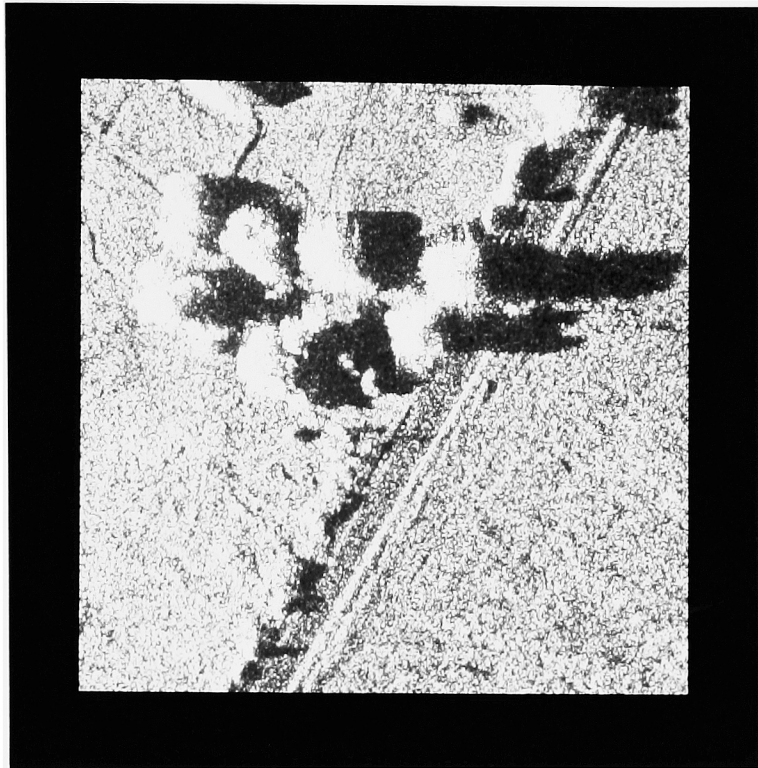


Figure 3-1 Image 4 (Equalized)

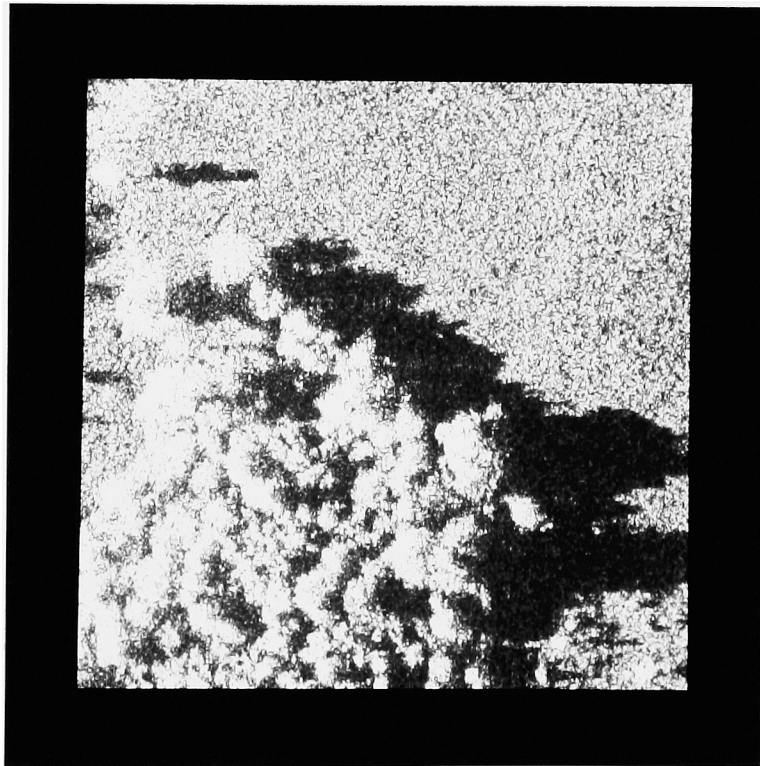


Figure 3-2 Image 9 (Equalized)

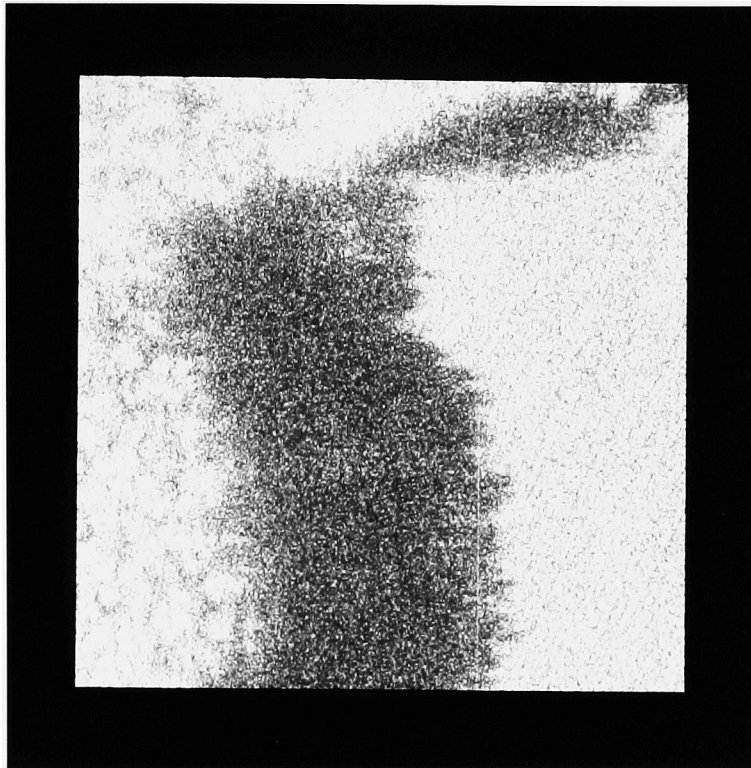


Figure 3-3 Image 28 (Equalized)

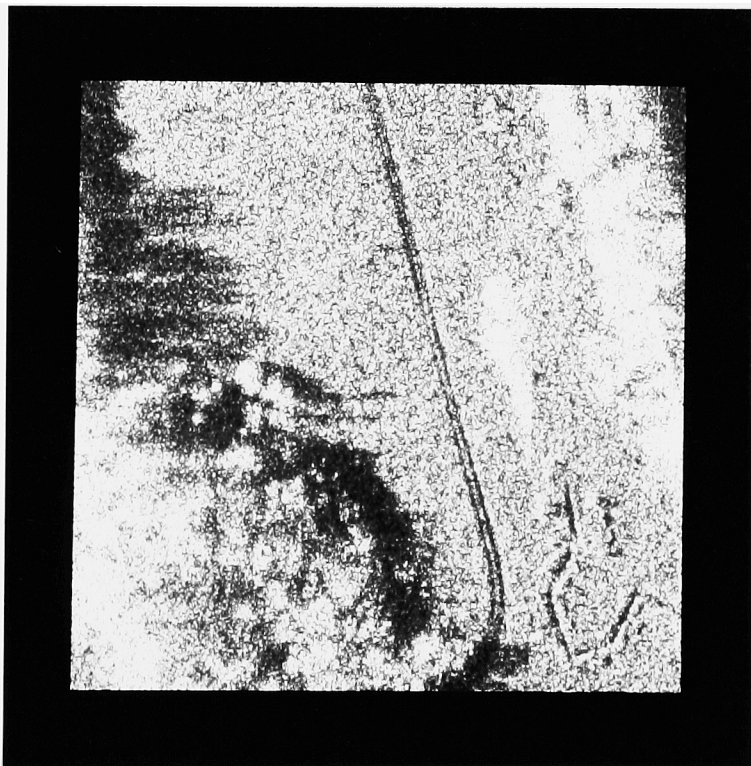


Figure 3-4 Image 29 (Equalized)

3.3 Image Preparation with the Stromberg Method

The procedure used to create the annular images using the Stromberg method followed closely that outlined in section 2.6 with only minor deviations. Because of the amount of noise in the imagery, selection of annuli was difficult. The original intent was to select annuli based on dominant frequencies which would be used to classify the image. However, the FFT outputs of the images looked very uniform and the magnitudes decreased with increased radial distance from image center as expected. Since no dominant frequencies were distinguishable, ten annular rings were chosen which covered the entire frequency domain image (512 x 512). Not all were used to classify the images. Section 3.5 explains the procedure for selecting annuli. The annular ring dimensions are shown in Table 3-1 and in Figure 3-5.

These radii were chosen to equalize the power within the annuli. As a result, the annular width steadily increases toward higher frequencies. The inner radius of Annulus 1 is 5 pixels in order to eliminate the lowest frequencies, including the DC, which were thought to be meaningless in this study of texture. The tenth annulus ten was added to analyze the frequencies from the corners of the transformed image.

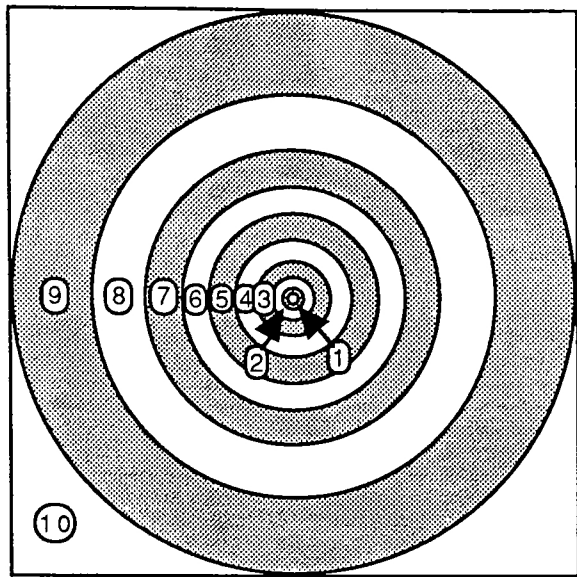


Figure 3-5 Illustration of Annular Ring Dimensions

Table 3-1 Annular Ring Dimensions

ANNULUS #	WIDTH (pixels)	RADIAL BOUNDARIES (pixels)	FREQUENCIES (ξ) (cycles/pixel)
1	5	5-10	.01-.02
2	10	10-20	.02-.04
3	15	20-35	.04-.07
4	20	35-55	.07-.11
5	25	55-80	.11-.16
6	30	80-110	.16-.21
7	35	110-145	.21-.28
8	50	145-195	.28-.38
9	60	195-255	.38-.50
10	105	255-360	.50-.70

Rather than use a binary lowpass filter, which would cause "ringing" (small oscillations near edges) in the space-domain image, a Butterworth lowpass filter was used. Similarly, a Butterworth bandpass filter was used instead of the binary annulus. The equation for the magnitude of the N^{th} order Butterworth lowpass filter is:

$$|H(\xi)| = \sqrt{\frac{1}{1 + (\xi / \xi_{co})^{2N}}} \quad (3-3)$$

where ξ_{co} is the nominal cutoff frequency at which the amplitude drops to $1/\sqrt{2}$. Also, the fall off of the function increases as the order N increases (Oppenheim, 1975) as Figure 3-6 illustrates.

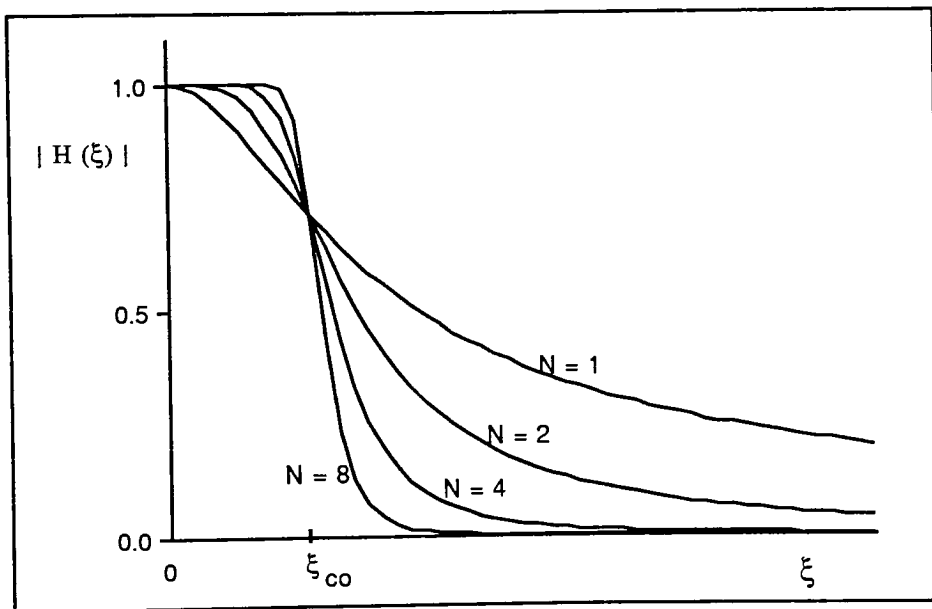


Figure 3.6 Dependence of Butterworth Lowpass Filter Magnitude on the Order N .

Testing was performed on a uniformly gray image to select the order for both of the Butterworth filters. The filter shape resembles a Gaussian in its slope and it does not extend far beyond the annular ring cutoff. The cutoff frequency used for each lowpass filter was the outermost frequency of that annulus, listed in Table 3-1. Order $N = 5$ was chosen for the lowpass filter because it is sufficiently steep at the highest frequencies needed for the high-frequency annular images, yet it did not fail during computation. In the case of annulus 9, the lowpass filter encompassed nearly the entire frequency-based image in order to capture the modulation function created by the annular ring.

Similar testing was performed for the Butterworth bandpass filter. Order $N=4$ was chosen because it was the highest order that could be used to calculate all of the annuli. The two-dimensional bandpass filter is created by computing the difference of two lowpass filters with different cutoff frequencies. The Butterworth bandpass filter extends slightly farther outside the annulus than inside, just as is the case for a difference of Gaussian filters.

Because both filters in the frequency domain were Butterworth functions, it was decided that the box filter was not necessary. The slow fall off in the frequency domain was considered to be equivalent to space domain averaging. The result was that time was saved by eliminating a step.

The Stromberg procedure used in this study consisted of the following steps:

1. Compute the Fourier transform of the image,
2. apply the bandpass filter in the frequency domain using the Butterworth annulus,
3. compute the inverse Fourier transform (return to the space domain),
4. compute the absolute value,
5. compute the Fourier transform (now in the frequency domain),
6. apply the lowpass filter,
7. compute the inverse Fourier transform of the result. (frequency to spatial domain)

3.4 Image Preparation with the Easton Method

Two deviations were made from the original theory in implementing the Easton method of texture extraction from section 2.7: the summation of the windows in the frequency domain and the selection and shape of the filters used.

Since the information is duplicated every 180° in the frequency domain, only half of an annulus is useful. And because the frequency representation of the SAR images are quite uniform, it is apparent that all segments of a half-annulus should be incorporated into the procedure for this initial study. Rather than dividing a given annulus into its component squares, it was advantageous to partition the Butterworth-filtered annulus used in the Stromberg method into six pie-shaped sections. In this manner, the Gaussian shape on two of the four sides would minimize some of the potential ringing and a given pixel in the frequency domain would not be included in more than one window. Figure 3-6 shows the windows used. After isolating each annulus, the window was centered and inverse transformed. The magnitudes of each of the six images were then summed in the space domain to create the feature band image corresponding to that annulus. Figure 3-7 shows window #1 of the frequency domain just before the inverse transform.

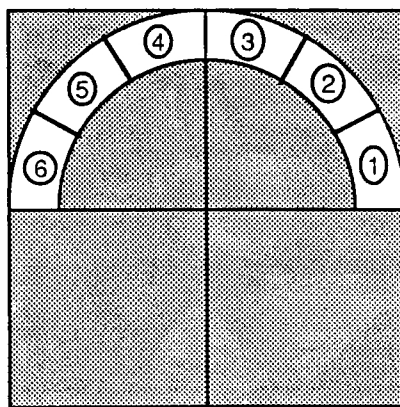


Figure 3-6 Example of Annulus Windows used in the Easton Method

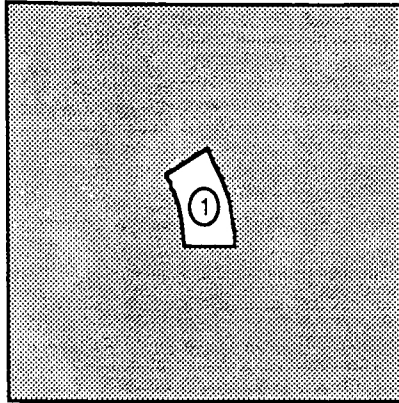


Figure 3-7 Example of a Centered Window of an Annulus

Since the same Butterworth function is used in both methods, there is no need to apply the box filter to average the images. The procedure used in this study consists of these steps:

1. Compute the Fourier transform of the image,
2. bandpass filter in the frequency domain using the Butterworth filter function to create an annulus,
3. isolate one of the six slices of the half annulus,
4. center that window in a new image,
5. compute the inverse Fourier Transform,
6. compute the magnitude of the image,
7. add to the other images from that annulus in the space domain,
8. go to step 3 until all segments have been used.

3.5 Analysis of the Texture Extraction Methods

The focus of this research is a comparison of the Stromberg and Easton texture extraction procedures on the SAR images.

3.5.1 Annulus Selection

In section 3.3, the rationale for selecting the set of annuli was discussed. Table 3-1 and Figure 3-5 show the specific dimensions for each of the ten annuli. However, the number of bands which may be used by the classification software is limited. As a result, only five of the ten annuli were chosen as input bands, along with the original 512 x 512 SAR image, to make a total of six bands. The same frequency bands were used to classify the images using both texture extraction methods.

To assist in selection of annuli, the correlation matrices for all bands were calculated using the principle component function in the ERDAS package software to derive variance/covariance matrices. Correlation coefficients were then calculated for the original image and the first nine annular feature images by the equation:

$$\rho_{xy} = \frac{\text{COV}[x,y]}{\sqrt{\text{VAR}[x] \text{VAR}[y]}} \quad (-1.0 \leq \rho_{xy} \leq 1.0) \quad (3-4)$$

when x and y represent any two of the ten image bands.

The correlation coefficients for the annuli of both texture extraction methods for the four images in this study are included in Appendix D. The goal was to select a set of annuli with a reasonable variation of frequencies and that minimized correlation coefficients. The latter restriction ensures that the maximum information content is available for the

classification process. If two bands are very highly correlated ($\rho \approx \pm 1.0$), then the second band adds little new information to the process.

Not surprisingly, analysis of the correlation matrices shows that the highest correlation for a given annulus exists in neighboring annuli. With this in consideration, annuli 1,3,5,7,and 9 were chosen to test the classification accuracy of the Stromberg and Easton texture extraction methods.

3.5.2 Image Classification

The four images in this study were classified using the Gaussian Maximum Likelihood (GML) classifier in the ERDAS software package. Basic classes were identified as grass, trees, and shadows on all four images. Two images (numbers 4 and 29) also contain a road, which is the fourth class. To perform the supervised training of each image, dependent polygons were chosen which accurately represent the texture within a class. In all cases, at least two polygons of significant size (350 pixels to 2000+ pixels) were chosen for each class. Class statistics were then calculated in ERDAS to allow pixel-by-pixel classification. Results within a class were then merged to create final class maps.

3.5.3 Classification Accuracy using Independent Polygons

After creating the class statistics and class maps for the entire image, new "independent" polygons were chosen from each image to test the classification maps. Consistent with the use of the dependent polygons, the same set of independent polygons was used for both the Easton and Stromberg feature extraction methods for a given image. These independent polygons were chosen in similar fashion to the dependent polygons, but

no pixels were in common between the two sets in order to accurately test the classifier. All polygons were chosen from the equalized images (shown in Figures 3-1 to 3-4). Overall classification accuracy was calculated by weighing the individual class accuracies by the class area within the image. This was obtained during the creation of the class map.

3.5.4 Classification Accuracy using Random Pixels

Classification tests with independent polygon only determine the classification success within the polygons. A more rigorous test was performed by choosing pixels at random for classification. This test used the RANDCAT function within ERDAS and is performed by the operator who makes a visual decision of the class to which each pixel belongs. The ERDAS software weights the number of pixels in each class based on the class map, in similar fashion to the weighting of overall independent polygon classification accuracy for each image. While this random pixel method is more tedious than other tests of classification accuracy, it does measure the success of the classification over the entire image. However, it is sometimes difficult for the operator to classify a pixel. In such cases, the pixel was not used. Fewer than 10% of the pixels in a given test did not belong to a distinguishable class.

3.5.5 Statistical Comparison

To accurately compare the two texture extraction methods, the random pixel classification results were used in a statistical test. A test of proportions (Dougherty, 1990) was used to test the null hypothesis that the Easton method of texture extraction is as good as (or better than) the Stromberg method. The test of this hypothesis is set up as follows:

$H_0 : p_E - p_S \geq 0$ (Easton's method is as good or better than the Stromberg's)

$H_1 : p_E - p_S < 0$ (Easton's method is not as good as Stromberg's)

$\alpha = 0.05$

$Z_{\text{crit}} = Z_{\alpha=0.05} = -1.645$

test statistic:
$$Z = \frac{\hat{p}_E - \hat{p}_S}{\sqrt{(\hat{p})(\hat{q})\left(\frac{1}{n_E} + \frac{1}{n_S}\right)}}$$

H_0 : the null hypothesis

H_1 : the alternative hypothesis

α : alpha risk - the probability of concluding H_1 when H_0 is true

\hat{p}_E : Easton method classification accuracy ($0 \leq \hat{p}_E \leq 1.0$)

\hat{p}_S : Stromberg method classification accuracy ($0 \leq \hat{p}_S \leq 1.0$)

\hat{p} : pooled estimate of p is the weighted average of the individual estimators

$$\hat{p} = \frac{n_E \hat{p}_E + n_S \hat{p}_S}{n_E + n_S} \quad \hat{q} = 1 - \hat{p}$$

n_E : number of samples in the test to obtain \hat{p}_E

n_S : number of samples in the test to obtain \hat{p}_S

In this case, the proportions are the classification accuracies. A proportion is described as the number of pixels correctly classified divided by the total number of pixels classified. Since not all pixels are sampled in the test, \hat{p}_E and \hat{p}_S are considered estimates of the population proportions p_E and p_S (the true classification accuracies of the two methods over the entire image). This test is valid only if the sample size is "large" enough to assume normality so that the Central Limit Theorem may apply. Opinions about the appropriate sample size vary. In these tests, the samples (n_E and n_S) contain 100 pixels which is sufficient to assume normality.

3.5.6 Implementation Comparison

Since all of this research used computer systems and software packages, a general comparison of the implementation of both the Easton and the Stromberg texture extraction methods has been performed based on the software and hardware used. In addition, an assessment was made of possible optical implementations.

4.0 RESULTS

4.1 Overview of the Stromberg and Easton Methods

Visual analysis of intermediate steps of each texture extraction procedure leads to results which differ from predictions, possibly because of image noise. Theoretically, a region (class) will produce brighter returns in some annular images than in others because classes are comprised of a unique variety of frequencies. The brightness will be greater if some of the frequencies are prevalent in the annulus of interest. Conversely, the pixels will be darker in that region of the space-domain bandpass-filtered image where few or none of the frequencies that make up a class have been isolated in the annulus. Addition of textural classes containing different frequencies provides for many different combinations of brightnesses when considering the entire set of annular feature images. The GML classifier can accurately segment the image based on those consistent variations.

Because of the presence of image noise, this theory of texture extraction as explained was not demonstrated for visual inspection. Figures 4-1, 4-2, and 4-3 show images obtained after most steps of both the Stromberg and Easton methods. Each shows image formation for annulus #7 (Table 3-1) which includes the band of frequencies (ξ) in the range of 0.21 to 0.28 cycles per pixel. One can see that the greatest brightness in each image occurs in the tree regions and the least brightness in the shadow regions, much like the original image. Figures 4-4 and 4-5 show each image used to classify Image 9 by both methods. Although the dynamic range of these images was maximized for display purposes, the relative brightnesses of each class are very similar from one annulus image to the next. This will result if the image noise also varies with brightness.

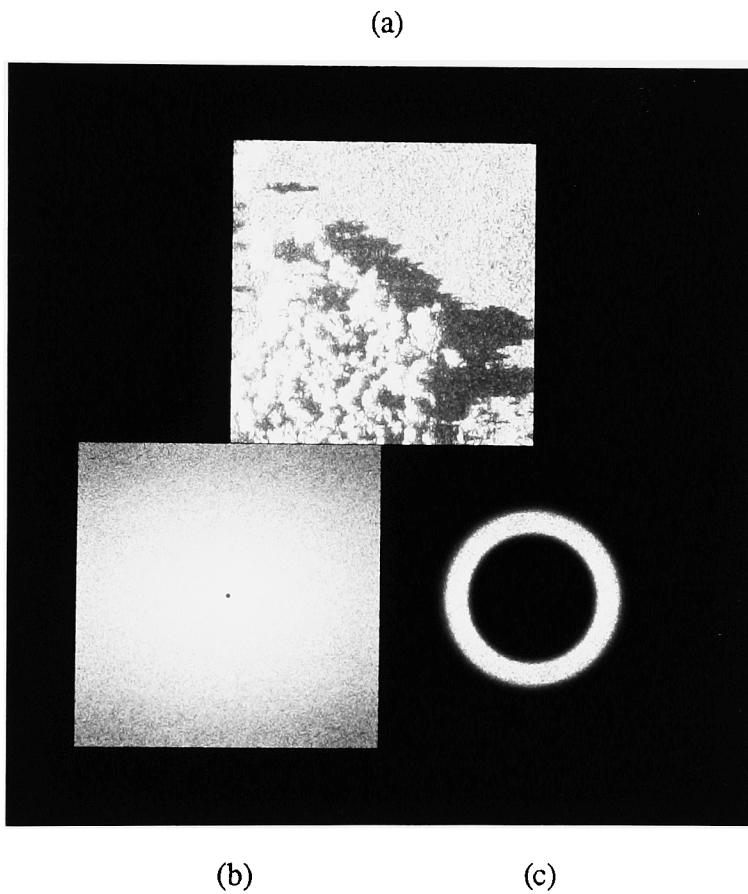


Figure 4-1 Initial Steps in the Formation of an Annulus Image (from Image 9) by the Stromberg and Easton Methods

(a). Original Image 9 (equalized)
(b). FFT of Original Image (c). Annulus 7 of FFT

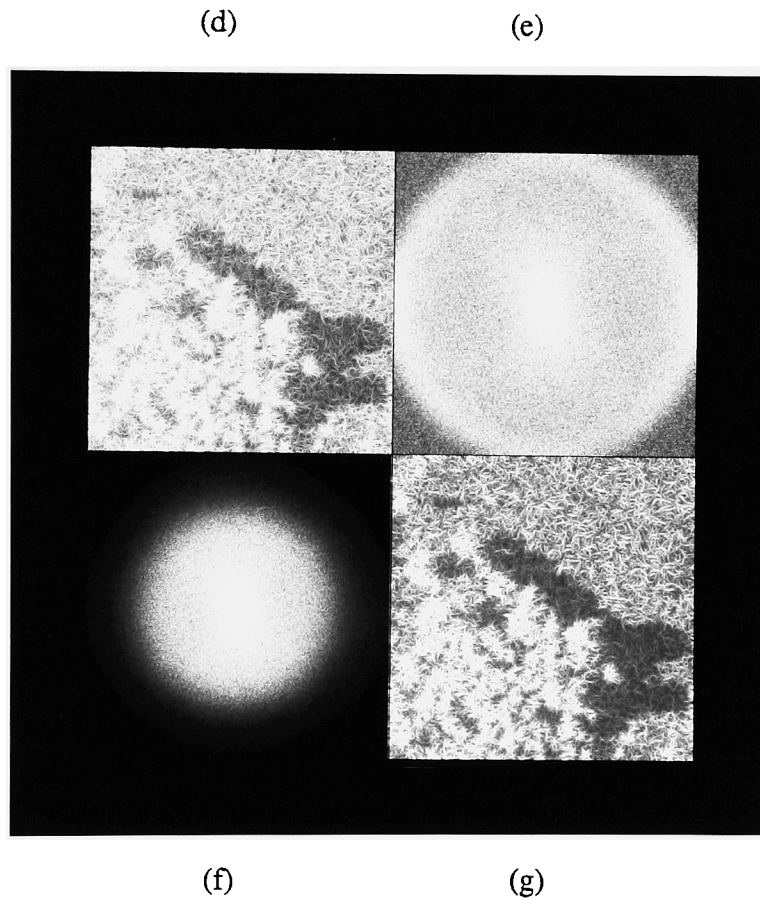


Figure 4-2 Final Steps in the Formation of an Annulus Image (from Image 9) by the Stromberg Method

-
- (d) Magnitude of Inverse FFT of Annulus 7
 - (e) FFT of (d)
 - (f) Low-pass Filter of (e)
 - (g) Inverse FFT of (f) - Final Annulus 7 Image

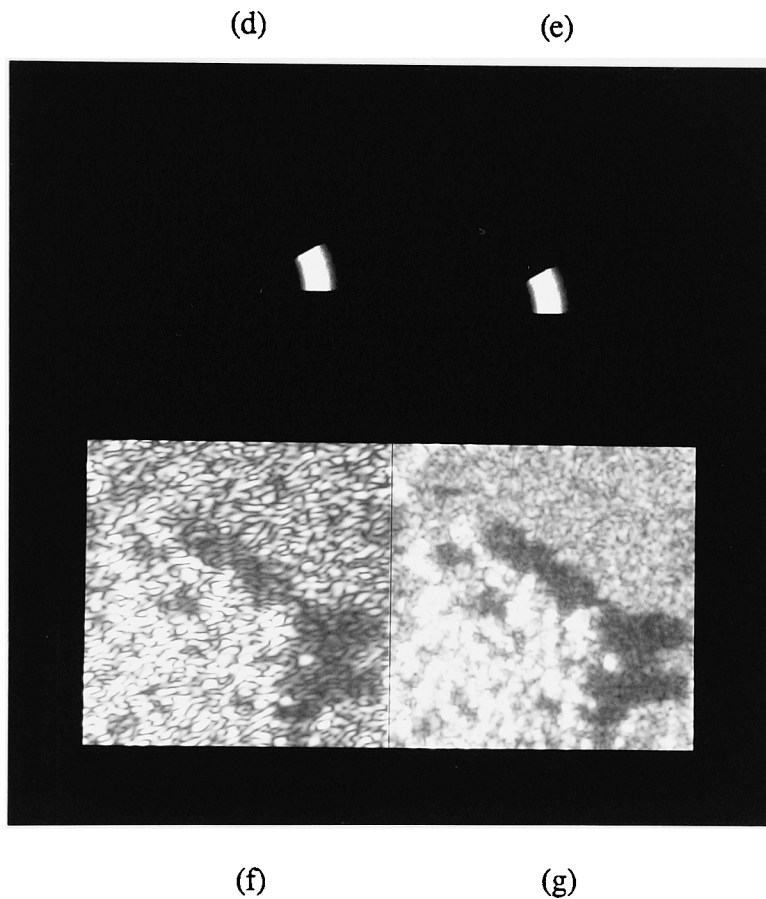


Figure 4-3 Final Steps in the Formation of an Annulus Image (from Image 9) by the Easton Method

-
- | | |
|-----------------------------------|--|
| (d). Window of Annulus 7 | (e). Centered Window of Annulus 7 |
| (f). Magnitude Inverse FFT of (e) | (g). Summation of Window Images (f)
(Final Annulus 7 Image) |

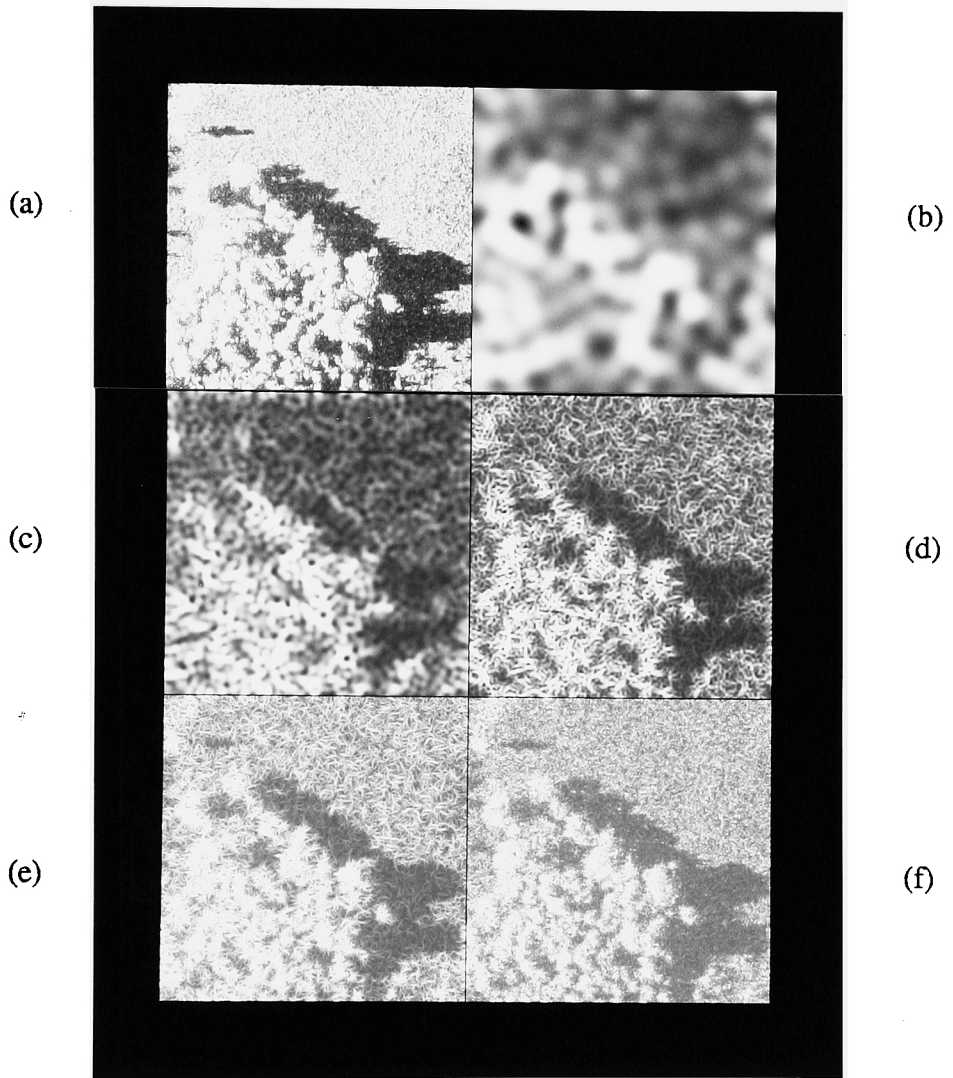


Figure 4-4 Final Annulus Images Created from Image 9 using the Stromberg Method

-
- | | |
|----------------------|---------------------|
| (a) Original Image 9 | (b) Annulus 1 Image |
| (c) Annulus 3 Image | (d) Annulus 5 Image |
| (e) Annulus 7 Image | (f) Annulus 9 Image |

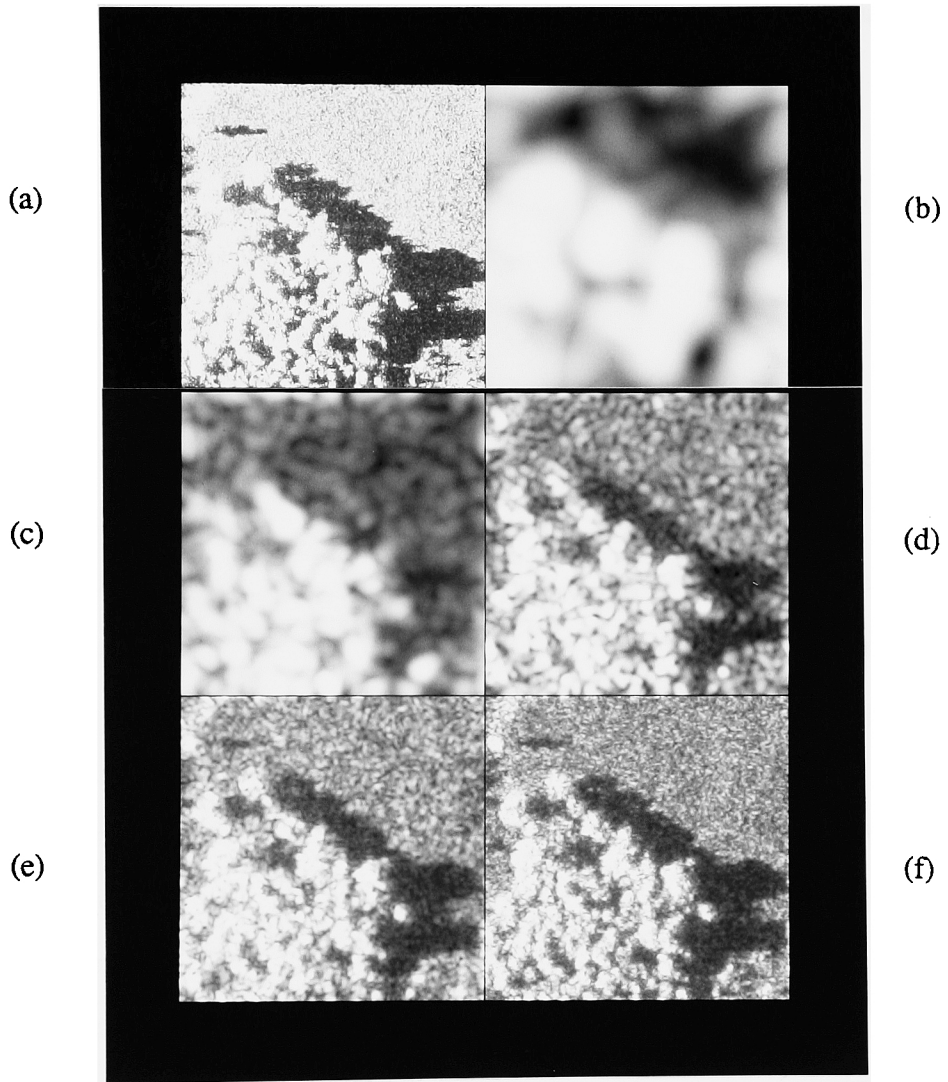


Figure 4-5 Final Annulus Images Created from Image 9 using the Easton Method

-
- | | |
|----------------------|---------------------|
| (a) Original Image 9 | (b) Annulus 1 Image |
| (c) Annulus 3 Image | (d) Annulus 5 Image |
| (e) Annulus 7 Image | (f) Annulus 9 Image |

The frequency representation of Image 9 shows that noise is present at all frequencies. It is difficult to pick out bright features at any frequency [Figure 4-1 (b)]. In addition, the noise appears to be directly correlated with brightness. In this manner, the brightest region (the trees), contains more amplitudes of all frequencies and is therefore brighter in each annular image, shown in Figures 4-4 and 4-5.

Analysis of different regions of one of the images backed the observation that the noise is multiplicative. Class regions were isolated to test this observation. The space domain region of trees had a higher mean and higher standard deviation than did grass or shadow. FFT's of each region were also analyzed. They showed that the tree area had the highest mean pixel level (after ignoring the DC value) meaning more of all frequencies present. Predictably, grass was next highest and shadows were last.

While this seems to dominate the display of the images, it does not necessarily dominate the classification. The noise may not totally overwhelm image information at the frequencies that should be isolated by each annulus. It is possible that the frequencies dominant in each texture class bias the noise frequency characteristics enough that the classification process can continue to detect differences. For instance, while the trees are brighter than other classes in two annulus images, they may be comparatively brighter in one because many underlying frequencies present in the trees were isolated in that annulus and not the other. While these changes may not be visibly detectable, the GML classification process should distinguish the differences. The results of the classification indicate reasonable success after considering the amount of noise present in the imagery.

4.2 Independent Polygon Classification Results

Independent polygon classification was explained in section 3.5.3. Table 4-1 shows the summary of those tests. Appendix B shows a more complete summary of the same results. The overall accuracy (in bold) is the most common result used for comparison. Overall accuracy is an estimate of the classification accuracy for that method over the entire image. Though often computed by averaging the individual class accuracies, the overall accuracy in this study is computed by weighting class accuracies by the individual class proportions of the entire image. While class weights are derived from the imprecise classification routine, the results are clearly better in this case than would be obtained by simply averaging weights of classes which do not contain approximately equal areas.

Figure 4-6 shows the classification maps of Image 9 and the original Image 9. In the classification maps, the classes are portrayed as different gray levels. From these results both methods classified Image 9 generally well. However, the accuracies listed in Table 4-1 are quite high and can be misleading without more information about how the numbers were derived. These classification accuracies significantly depend on the location of the independent polygons. Though chosen in similar fashion to the dependent polygons used for the training set, the overall accuracy can nevertheless vary for different texture extraction methods even though the same polygons are used for both methods. If the polygons were chosen in areas that were classified well by that method, the accuracy will be higher than if not.

Figure 4-7 displays the Image 4 class maps and the original Image 4 for comparison. The accuracy of both methods decreases with the addition of the road class (Images 4 and 29). The results for both the class maps and the numeric results reinforce

that conclusion. It is clear from Figure 4-7 that the Stromberg method classifies better with the addition of the road class. However a firm statistical conclusion cannot be made from the independent polygon statistics. In this study, only the random pixel classification will be used for the final statistical judgement.

Table 4-1
Summary of Independent Polygon Classification Results (percentages)

<u>IMAGE</u>	<u>METHOD</u>	<u>GRASS</u>	<u>TREE</u>	<u>SHADOW</u>	<u>ROAD</u>	<u>OVERALL</u>
4	Stromberg	99.9	100.0	96.1	24.5	86.1
4	Easton	86.6	100.0	81.4	37.1	79.9

9	Stromberg	99.7	100.0	99.8	----	99.8
9	Easton	100.0	100.0	100.0	----	100.0

28	Stromberg	93.2	97.7	99.1	----	96.1
28	Easton	100.0	100.0	100.0	----	100.0

29	Stromberg	99.0	97.9	73.9	63.5	87.6
29	Easton	93.6	99.4	55.5	39.2	78.1
=====						
* PERCENTAGE CLASSIFICATION AREA OF IMAGE (used for overall accuracy)						
4		56	19	7	18	
9		58	25	17	--	
28		42	35	23	--	
29		37	25	23	15	
* based on average of areas from the class maps of each method for an image						

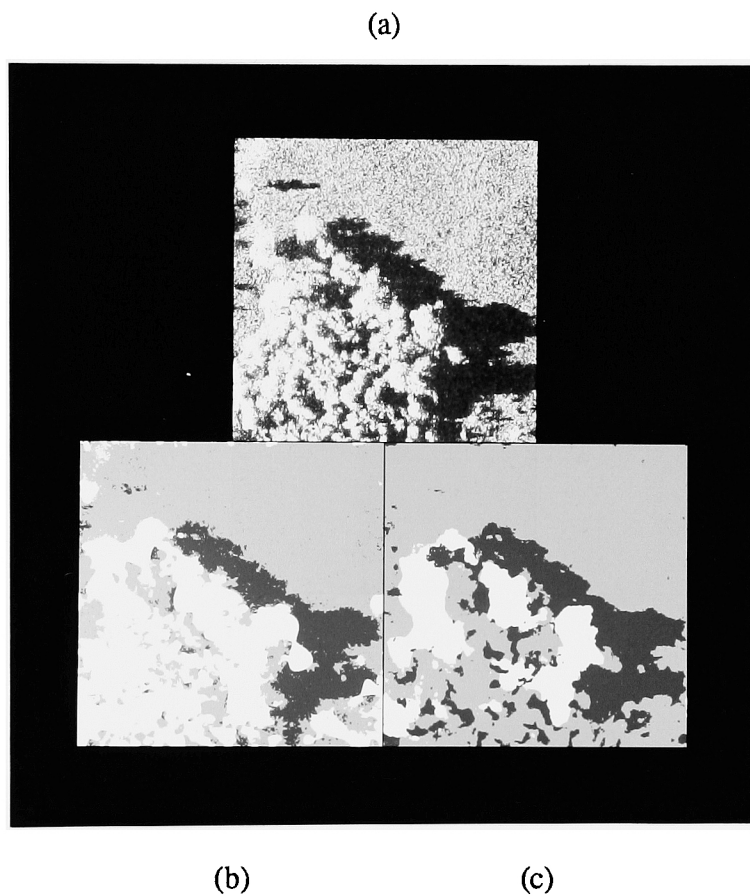


Figure 4-6 Classification Maps of Image 9 Compared to Original Image 9

(a) Original Image 9
(b) Stromberg Method Class Map (c) Easton Method Class Map

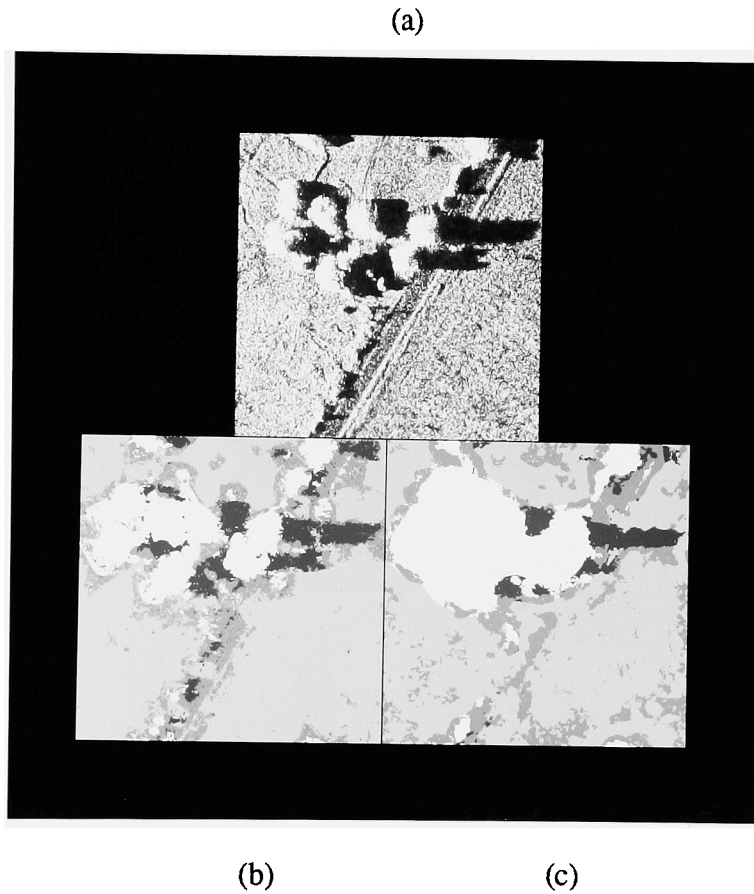


Figure 4-7 Classification Maps of Image 4 Compared to Original Image 4

(a) Original Image 4

(b) Stromberg Method Class Map

(c) Easton Method Class Map

4.3 Random Pixel Classification Results

The process of random pixel classification was explained in Section 3.5.4. Table 4-2 outlines the results and a complete tabulation is given in Appendix C.

As explained above, random pixel classification is a better test of overall accuracy for a classification technique because it does not exclude areas of the image from testing, while the independent classification accuracy includes only those pixels inside the chosen polygon. The ERDAS software selects pixels randomly from throughout in the image and allows the human operator to determine the true class for each pixel if possible. The human selection process may result in some error, but random pixel classification is a very unbiased method to estimate overall classification accuracy and therefore useful for a statistical hypothesis test.

The results show somewhat less success than the independent polygon results, mainly because of the pixel sampling previously explained. Again, the images with road present performs worse than those without. While the individual class success is reasonable for roads in image Image 4 and 29, it is based on fewer pixels and does not directly affect the overall accuracy as do the other classes because of its weight. However, the indirect affect that roads have on classification success is more significant. The classification accuracy of grass decreases considerably with the addition of the road class. Success of the classification of grass ranges from 65.3% to 78.1% with roads and 84.2% to 100.0% without roads in the image.

The overall accuracies were then used in a statistical test of proportions. They clearly show that the Stromberg method is not better than the Easton method of feature extraction. Table 4-3 shows the specific test and the results for each of the four images in this test.

Table 4-2
 Summary of Random Pixel Classification Results
 (percentages)

<u>IMAGE</u>	<u>METHOD</u>	<u>GRASS</u>	<u>TREE</u>	<u>SHADOW</u>	<u>ROAD</u>	<u>OVERALL</u>
4	Stromberg	78.1	66.7	47.6	66.7	71.0
4	Easton	76.1	75.0	25.0	80.0	66.0

9	Stromberg	100.0	79.2	38.2	----	74.0
9	Easton	93.2	48.0	64.5	----	73.0

28	Stromberg	84.2	87.5	65.8	----	78.0
28	Easton	86.7	86.2	61.0	----	76.0

29	Stromberg	69.6	82.6	46.2	80.0	67.0
29	Easton	65.3	77.3	78.6	100.0	72.0
=====						
* PERCENTAGE TOTAL CLASSIFICATION MAP (used for overall accuracy weights)						
4	Stromberg	73	3	21	3	100.0
4	Easton	67	8	20	5	100.0

9	Stromberg	42	24	34	--	100.0
9	Easton	44	25	31	--	100.0

28	Stromberg	38	24	38	--	100.0
28	Easton	30	29	41	--	100.0

29	Stromberg	46	23	26	5	100.0
29	Easton	49	22	28	1	100.0

* based on computer generated weights used in pixel selection						

4.4 Statistical Test Results from the Random Pixel Classification

Table 4-3

Hypothesis Test of Proportions on Random Pixel Classification Results

$H_0 : p_E - p_S \geq 0$ (Easton's method is as good or better than Stromberg's)

$H_1 : p_E - p_S < 0$ (Easton's method is not as good as Stromberg's)

$\alpha = 0.05$

$Z_{crit} = Z_{\alpha=0.05} = -1.645$

test statistic:
$$Z = \frac{\hat{p}_E - \hat{p}_S}{\sqrt{(\hat{p})(\hat{q})\left(\frac{1}{n_E} + \frac{1}{n_S}\right)}}$$

\hat{p}_E : Easton method classification accuracy ($0 \leq \hat{p}_E \leq 1.0$)

\hat{p}_S : Stromberg method classification accuracy ($0 \leq \hat{p}_S \leq 1.0$)

\hat{p} : pooled estimate of p is the weighted average of the individual estimators

$$\hat{p} = \frac{n_E \hat{p}_E + n_S \hat{p}_S}{n_E + n_S} \quad \hat{q} = 1 - \hat{p}$$

$n_E = 100$ number of samples in the test to obtain \hat{p}_E

$n_S = 100$ number of samples in the test to obtain \hat{p}_S

IMAGE	\hat{p}_S	\hat{p}_E	Z	DECISION *
4	0.71	0.66	-0.76	Do Not Reject the Null Hypothesis (H_0)
9	0.74	0.73	-0.16	Do Not Reject the Null Hypothesis (H_0)
28	0.78	0.76	-0.34	Do Not Reject the Null Hypothesis (H_0)
29	0.67	0.72	+0.65	Do Not Reject the Null Hypothesis (H_0)

* Decision based on comparison of Z statistic to the critical Z value ($Z_{crit} = -1.645$)
 Reject H_0 if and only if $Z \leq -1.645$.

4.5 Digital Implementation Comparison

Both the Stromberg and Easton texture extraction methods were implemented and tested on the VAX 4000 computer system. Both methods are computationally intensive primarily because of the FFT of 512 x 512 images. Since they are so similar, the only way to compare the computation of the two methods is by time required.

The Stromberg method requires four FFT operations and two Butterworth operations per annulus image. The total for five annulus images is 20 FFT operations and 10 Butterworth filter operations.

The Easton procedure originally involved fewer steps than its later versions. Additional time was required when combining selected frequency windows was found to be advantageous in the space domain, after computing the magnitude. This was to avoid the possibility that phase information could be lost when frequency windows are translated and summed or when space domain images are summed before the magnitude is computed. As a result, one forward transform, one Butterworth filter, and six inverse FFT's are required to produce images from six segments of one annulus. The total for producing 5 annulus images is 35 FFT operations and 5 Butterworth filter operations, although a smaller FFT operation could be used depending on segment (window) size.

While the Easton method involves 5 fewer Butterworth filter operations, it is more time consuming as a result of 15 more FFT operations if done on full frames. Both procedures required similar computation times of about 15 seconds. Therefore the totals can be pooled to conclude that the Easton method requires 10 more filter/transform operations to produce 5 annulus images than the Stromberg method requires. Based on unscientific testing during this research, that translates to 2 minutes and 30 seconds total time or roughly 30 seconds per annulus image advantage for the Stromberg method.

5.0 CONCLUSIONS

A procedure for Fourier-based textural feature extraction has been introduced and implemented in this study . It has been tested against the older Stromberg method. Both methods rely on the theory that regions of an image can be segmented based on texture differences and that these differences can be revealed by isolating the underlying frequency components of each texture. Both procedures isolate these frequencies by bandpass filtering in the Fourier domain. The Stromberg method uses the absolute value operator in the space domain followed by a lowpass filter in the frequency domain to produce an annulus image. The set of bandpass-filtered images is used for classification. The Easton method avoids the second transform into the frequency domain by isolating windows within the annulus (pass band). Each window is centered, inverse transformed, and the magnitude is computed. The images from each segment are summed to create the bandpass-filtered images.

The two methods were implemented and tested on the same four simple synthetic aperture radar (SAR) images. Two contain only grass, trees, and shadow classes while the other two add a road class. The goal of the research was to demonstrate both techniques on basic SAR images and to test if the Stromberg method is better than the Easton method based on those tests.

Based on the statistical results, it is clear that both texture extraction methods performed reasonably well. Both methods yielded accuracies from 66% to 72% on the images that contain road classes, and 73% to 78% on the images without road classes. All four statistical hypothesis tests concluded that the Stromberg method cannot be considered better than the Easton method with alpha risk equal to 0.05 based on a random sample size of 100 from each image.

This study was developed to show that classification of SAR imagery with the Stromberg and Easton methods can be implemented on digital computers with a reasonable processing time. Little effort was made to filter the image noise prevalent in the SAR imagery. The two methods were tested against each other statistically and an assessment was made on each concerning their computer implementations. Recommendations on any potential optical implementations are included in section 6.0.

6.0 RECOMMENDATIONS

This study had very general objectives since it was intended to test a new concept that has not been tested on real SAR imagery. As a result, it leaves unanswered questions which can be topics of further study.

The affects of image noise were ignored in this study, but might be the limiting factor to significant improvement of either the Stromberg or Easton texture extraction methods in classifying SAR imagery. It is difficult to determine the extent to which noise affected the testing even though analysis showed the noise to be multiplicative. However, it is reasonable to conclude that classification accuracy was decreased significantly because of noise. Since noise seems to be so prevalent in SAR imagery, more research should address the general problem. A relatively noise-free panchromatic image was classified using both methods implemented in this study. Results from the training data show equally good success compared to the SAR imagery, although the image scale differed.

A different method for selection of pass bands could be used. If image noise is treated similarly to its treatment in this study, more testing could lead to conclusions about the relative importance of different annuli. Individual annuli can be examined more closely for underlying frequency changes within the noise.

Window selection in the Easton method is also an area for possible improvement. In this study, each half annulus was segmented into six windows. Any reduction in the number of windows eliminates one inverse transform, one magnitude calculation, and one summation. Obviously, there is a time incentive to minimize the required number of segments in a passband to accurately isolate the desired frequencies. It would be interesting to examine the image obtained from each segment for differences. One could then analyze different summations of the six segments. There are only 15 combinations of segment pairs, 20 combinations of three, and another 15 additional sets of four.

It would be very interesting to create 512 x 512 synthetic SAR images to test these methods. Noise could be added if needed to test a theory but could be more easily eliminated if so desired. In this way, threshold testing could lead to an automated method of annulus selection that could be implemented on the real imagery.

Some of these same synthetic images, and eventually real SAR images, could also be segmented optically using the theories implemented digitally. The Stromberg textural feature extraction method is difficult to implement optically because of the absolute value operation. This is a nonlinear process that can only be simulated in an optical system by square law detection with a detector array or photographic film.

The Easton textural feature extraction method can be performed optically much more simply because it requires only three optical processes and no intermediate square law detection. The system requires a Fourier transform, an amplitude filter, and an inverse Fourier transform. The filter can be implemented optically by using either a binary transparency or a liquid crystal light valve. The size of the system is roughly four focal lengths. The output image is inverted because of the nature of the Fourier optics. The feature images thus generated could be produced much more quickly than the computer processed imagery. The output may be digitized, stored, and digitally combined.

In addition, the digital implementation could eliminate the centering of the window. Since the magnitude is used in the space domain (like intensity in the optical implementation), the window centering is unnecessary in the Easton method. Appendix F shows an example. The result is the same as that shown in Figure 2-7. This would save time and it would more accurately simulate the optical implementation.

REFERENCES

Bessette, L.A., R.M.Barnes, S.C.Crocker, C.E.Frost, L.E.Guthrie, Project Report TT-80: "Stockbridge Mission 85 Pass 5 Data Package, Lincoln Laboratory, Massachusetts Institute of Technology, Lexington, MA, 8 MAY 1991.

Burl, Michael C., Gregory J. Owirka, Leslie M. Novak, "Texture Discrimination in Synthetic Aperture Radar Imagery", Twenty-Third Asilomar Conference on Signals, Systems, and Computers, Conference Record, pp. 399-404, 30 Oct-1 Nov 1989.

Burns, Barbara A. and David R. Lyzenga, "Textural Analysis as a SAR Classification Tool", *Electromagnetics*, Vol. 4:309-322, 1984.

Castleman, Kenneth R., Digital Image Processing, Prentice-Hall Inc., Englewood Cliffs, New Jersey, 1979, pp. 2-9.

Dougherty, Edward R., Probability and Statistics for the Engineering, Computing, and Physical Sciences, Prentice-Hall Inc., Englewood Cliffs, New Jersey, 1990, pp. 280-283.

ERDAS User's Guide, copyright (c) 1988, by ERDAS, Inc., Atlanta, GA.

Haralick, Robert M., K. Shanmugam, and Its'hak Dinstein, "Textural Features for Image Classification", *IEEE Transactions on Systems, Man, and Cybernetics*, Vol. SMC-3, No. 6, November, 1973.

Holecz, F., E. Meier, Ch. Graf, and D. Nuesch, "Textural Analysis Applied To Geocoded SAR Images", International Geoscience and Remote Sensing Symposium, V. 5, July, 1989, pp. 2789-2793.

Holmes, Quentin A., Daniel R. Nuesch, and Robert A. Shuchman, "Textural Analysis and Real-Time Classification of Sea-Ice Types Using Digital SAR Data", *IEEE Transactions on Geoscience and Remote Sensing*, Vol. GE-22, No. 2, March 1984, pp. 113-120.

Laur, H., T. Le Toan, A. Lopes, "Textural Segmentation of SAR Images using First Order Statistical Parameters", Proceedings of IGARRS 1987 Symposium, Ann Arbor, MI, 18-21 May, 1987, pp. 1463-1468.

Lillesand, Thomas M., and Ralph W. Kiefer, Remote Sensing and Image Interpretation, John Wiley & Sons, New York, 1987.

Oppenheim, Alan V., and Ronald W. Schaffer, Digital Signal Processing, Prentice-Hall, Englewood Cliffs, New Jersey, 1975, pp. 211-218.

Robert, Denis J., "Selection and Analysis of Optimal Textural Features for Accurate Classification of Monochrome Digitized Image Data", *MS Thesis*, Rochester Institute of Technology, Rochester, New York, 1989.

Rosenblum, W.I., "Optimal Selection of Textural and Spectral Features for Scene Segmentation", *MS Thesis*, Rochester Institute of Technology, Rochester, New York, 1990.

Schowengerdt, Robert A., Techniques for Image Processing and Classification in Remote Sensing, Academic Press, New York, 1983.

Stein, Jess, Editor in Chief, The Random House College Dictionary, Revised Edition, Random House Inc., 1980.

Stromberg, William.D. and Tom G. Farr, "A Fourier-based Textural Feature Extraction Procedure", *IEEE Transactions on Geoscience and Remote Sensing*, Vol. GE-24, No. 5, pp. 722-731, September, 1986.

Toomay, J.C., Radar Principles For the Non-Specialist, Lifetime Learning Publications, Belmont, California, 1982.

Ulaby, Fawwaz T., F. Kouyate, B. Brisco, and T.H. Lee Williams, "Textural Information in SAR Images", *IEEE Transactions on Geoscience and Remote Sensing*, Vol. GE-24, No. 2, March 1986.

APPENDIX A.

FEATURES LIST

(Rosenblum, 1990)

<u>Group #</u>	<u>Feature #</u>	<u>Feature Name</u>
Co-occurrence Features		
1	1.	Angular second moment average
	2.	Angular second moment range
2	3.	Contrast average
	4.	Contrast range
3	5.	Correlation average
	6.	Correlation range
4	7.	Variance average
	8.	Variance range
5	9.	Inverse difference moments average
	10.	Inverse difference moments range
6	11.	Sum average average
	12.	Sum average range
7	13.	Sum variance average
	14.	Sum variance range
8	15.	Sum entropy average
	16.	Sum entropy range
9	17.	Entropy average
	18.	Entropy range
10	19.	Difference entropy average
	20.	Difference entropy range
11	21.	Information measure of correlation A average
	22.	Information measure of correlation A range
	23.	Information measure of correlation B average
	24.	Information measure of correlation B range
12	25.	Difference variance average
	26.	Difference variance range
13	27.	Maximum probability average
	28.	Maximum probability range

<u>Group #</u>	<u>Feature #</u>	<u>Feature Name</u>
----------------	------------------	---------------------

First-Order Statistics Features

14	29.	Gradient
15	30.	Mean Brightness
	31.	Variance
	32.	Brightness

Run Length Statistics Features

16	33.	Short run emphasis average
	34.	Short run emphasis range
	35.	Long run emphasis average
	36.	Long run emphasis range
	37.	Gray level non-uniformity average
	38.	Gray level non-uniformity range
	39.	Run length non-uniformity average
	40.	Run length non-uniformity range
	41.	Fraction of image in runs average
	42.	Fraction of image in runs range

Gray Level Difference Statistics Features

17	43.	Contrast
	44.	Angular second moment
	45.	Entropy
	46.	Mean

Spectral Information (not used in this study)

18	47.	Red Spectral Film Band
	48.	Green Spectral Film Band
	49.	Blue Spectral Film Band

APPENDIX B.

INDEPENDENT POLYGON CLASSIFICATION

IMAGE 4 - STROMBERG METHOD

CLASSIFIED AS:	TRUTH							
	GRASS		TREE		SHADOW		ROAD	
GRASS	4919	99.9%	0	0.0%	16	0.9%	785	68.7%
TREE	0	0.0%	1618	100.0%	2	0.1%	10	0.9%
SHADOW	3	0.1%	0	0.0%	1661	96.1%	67	5.9%
ROAD	0	0.0%	0	0.0%	50	2.9%	280	24.5%
TOTAL	4922		1618		1729		1142	

OVERALL ACCURACY 86.1%

IMAGE 4 - EASTON METHOD

CLASSIFIED AS:	TRUTH							
	GRASS		TREE		SHADOW		ROAD	
GRASS	4261	86.6%	0	0.0%	154	8.9%	683	59.8%
TREE	0	0.0%	1618	100.0%	26	1.5%	0	0.0%
SHADOW	0	0.0%	0	0.0%	1407	81.4%	35	3.1%
ROAD	661	13.4%	0	0.0%	142	8.2%	424	37.1%
TOTAL	4922		1618		1729		1142	

OVERALL ACCURACY 79.9%

NOTE: ACCURACY BASED ON WEIGHTS DERIVED FROM THE AVERAGE OF CLASS MAP AREAS FOR EACH CLASS FROM BOTH EASTON AND STROMBERG METHODS. THEY ARE:

GRASS	TREE	SHADOW	ROAD
0.56	0.19	0.07	0.18

INDEPENDENT POLYGON CLASSIFICATION

IMAGE 9 - STROMBERG METHOD

CLASSIFIED AS:	TRUTH					
	GRASS		TREE		SHADOW	
GRASS	2771	99.7%	0	0.0%	6	0.2%
TREE	0	0.0%	1131	100.0%	0	0.0%
SHADOW	9	0.3%	0	0.0%	2410	99.8%
TOTAL	2780		1131		2416	

OVERALL ACCURACY **99.8%**

IMAGE 9 - EASTON METHOD

CLASSIFIED AS:	TRUTH					
	GRASS		TREE		SHADOW	
GRASS	2780	100.0%	0	0.0%	0	0.0%
TREE	0	0.0%	1131	100.0%	0	0.0%
SHADOW	0	0.0%	0	0.0%	2416	100.0%
TOTAL	2780		1131		2416	

OVERALL ACCURACY **100.0%**

NOTE: ACCURACY BASED ON WEIGHTS DERIVED FROM THE AVERAGE OF CLASS MAP AREAS FOR EACH CLASS FROM BOTH EASTON AND STROMBERG METHODS. THEY ARE:

GRASS	TREE	SHADOW
0.58	0.25	0.17

INDEPENDENT POLYGON CLASSIFICATION

IMAGE 28 - STROMBERG METHOD

CLASSIFIED AS:	TRUTH					
	GRASS		TREE		SHADOW	
GRASS	4296	93.2%	53	2.3%	43	0.8%
TREE	307	6.7%	2236	97.7%	7	0.1%
SHADOW	8	0.2%	0	0.0%	5219	99.1%
TOTAL	4611		2289		5269	

OVERALL ACCURACY **96.1%**

IMAGE 28 - EASTON METHOD

CLASSIFIED AS:	TRUTH					
	GRASS		TREE		SHADOW	
GRASS	4611	100.0%	0	0.0%	0	0.0%
TREE	0	0.0%	2289	100.0%	0	0.0%
SHADOW	0	0.0%	0	0.0%	5269	100.0%
TOTAL	4611		2289		5269	

OVERALL ACCURACY **100.0%**

NOTE: ACCURACY BASED ON WEIGHTS DERIVED FROM THE AVERAGE OF CLASS MAP AREAS FOR EACH CLASS FROM BOTH EASTON AND STROMBERG METHODS. THEY ARE:

GRASS	TREE	SHADOW
0.42	0.35	0.23

INDEPENDENT POLYGON CLASSIFICATION

IMAGE 29 - STROMBERG METHOD

CLASSIFIED AS:	TRUTH							
	GRASS		TREE		SHADOW		ROAD	
GRASS	4473	99.0%	39	2.0%	214	9.3%	350	36.2%
TREE	0	0.0%	1898	97.9%	376	16.4%	2	0.2%
SHADOW	1	0.0%	0	0.0%	1695	73.9%	1	0.1%
ROAD	46	1.0%	1	0.1%	8	0.4%	614	63.5%
TOTAL	4520		1938		2293		967	

OVERALL ACCURACY **87.6%**

IMAGE 29 - EASTON METHOD

CLASSIFIED AS:	TRUTH							
	GRASS		TREE		SHADOW		ROAD	
GRASS	4231	93.6%	0	0.0%	985	43.0%	588	60.8%
TREE	0	0.0%	1927	99.4%	0	0.0%	0	0.0%
SHADOW	40	0.9%	11	0.6%	1273	55.5%	0	0.0%
ROAD	249	5.5%	0	0.0%	35	1.5%	379	39.2%
TOTAL	4520		1938		2293		967	

OVERALL ACCURACY **78.1%**

NOTE: ACCURACY BASED ON WEIGHTS DERIVED FROM THE AVERAGE OF CLASS MAP AREAS FOR EACH CLASS FROM BOTH EASTON AND STROMBERG METHODS. THEY ARE:

GRASS	TREE	SHADOW	ROAD
0.37	0.25	0.23	0.15

APPENDIX C.

RANDOM PIXEL CLASSIFICATION

IMAGE 4 - STROMBERG METHOD

CLASSIFIED DATA	TRUTH							
	GRASS		TREE		SHADOW		ROAD	
GRASS	57	78.1%	1	33.3%	2	9.5%	1	33.3%
TREE	4	5.5%	2	66.7%	6	28.6%	0	0.0%
SHADOW	0	0.0%	0	0.0%	10	47.6%	0	0.0%
ROAD	12	16.4%	0	0.0%	3	14.3%	2	66.7%
TOTAL	73		3		21		3	

OVERALL ACCURACY **71.0%**

IMAGE 4 - EASTON METHOD

CLASSIFIED DATA	TRUTH							
	GRASS		TREE		SHADOW		ROAD	
GRASS	51	76.1%	0	0.0%	4	20.0%	1	20.0%
TREE	6	9.0%	6	75.0%	10	50.0%	0	0.0%
SHADOW	0	0.0%	0	0.0%	5	25.0%	0	0.0%
ROAD	10	14.9%	2	25.0%	1	5.0%	4	80.0%
TOTAL	67		8		20		5	

OVERALL ACCURACY **66.0%**

RANDOM PIXEL CLASSIFICATION

IMAGE 9 - STROMBERG METHOD

CLASSIFIED DATA	TRUTH					
	GRASS		TREE		SHADOW	
GRASS	42	100.0%	5	20.8%	5	14.7%
TREE	0	0.0%	19	79.2%	16	47.1%
SHADOW	0	0.0%	0	0.0%	13	38.2%
TOTAL	42		24		34	

OVERALL ACCURACY **74.0%**

IMAGE 9 - EASTON METHOD

CLASSIFIED DATA	TRUTH					
	GRASS		TREE		SHADOW	
GRASS	41	93.2%	11	44.0%	10	32.3%
TREE	3	6.8%	12	48.0%	1	3.2%
SHADOW	0	0.0%	2	8.0%	20	64.5%
TOTAL	44		25		31	

OVERALL ACCURACY **73.0%**

RANDOM PIXEL CLASSIFICATION

IMAGE 28 - STROMBERG METHOD

CLASSIFIED DATA	TRUTH					
	GRASS		TREE		SHADOW	
GRASS	32	84.2%	3	12.5%	8	21.1%
TREE	6	15.8%	21	87.5%	5	13.2%
SHADOW	0	0.0%	0	0.0%	25	65.8%
TOTAL	38		24		38	

OVERALL ACCURACY **78.0%**

IMAGE 28 - EASTON METHOD

CLASSIFIED DATA	TRUTH					
	GRASS		TREE		SHADOW	
GRASS	26	86.7%	4	13.8%	9	22.0%
TREE	4	13.3%	25	86.2%	7	17.1%
SHADOW	0	0.0%	0	0.0%	25	61.0%
TOTAL	30		29		41	

OVERALL ACCURACY **76.0%**

RANDOM PIXEL CLASSIFICATION

IMAGE 29 - STROMBERG METHOD

CLASSIFIED DATA	TRUTH							
	GRASS		TREE		SHADOW		ROAD	
GRASS	32	69.6%	3	13.0%	5	19.2%	1	20.0%
TREE	5	10.9%	19	82.6%	6	23.1%	0	0.0%
SHADOW	3	6.5%	0	0.0%	12	46.2%	0	0.0%
ROAD	6	13.0%	1	4.3%	3	11.5%	4	80.0%
TOTAL	46		23		26		5	

OVERALL ACCURACY **67.0%**

IMAGE 29 - EASTON METHOD

CLASSIFIED DATA	TRUTH							
	GRASS		TREE		SHADOW		ROAD	
GRASS	32	65.3%	1	4.5%	4	14.3%	0	0.0%
TREE	2	4.1%	17	77.3%	1	3.6%	0	0.0%
SHADOW	5	10.2%	3	13.6%	22	78.6%	0	0.0%
ROAD	10	20.4%	1	4.5%	1	3.6%	1	100.0%
TOTAL	49		22		28		1	

OVERALL ACCURACY **72.0%**

APPENDIX D.

CORRELATION COEFFICIENT MATRICES

IMAGE 4 - STROMBERG METHOD

BAND	1	2	3	4	5	6	7	8	9	10
1										
2	0.72									
3	0.52	0.64								
4	0.45	0.49	0.55							
5	0.38	0.43	0.46	0.56						
6	0.31	0.39	0.42	0.50	0.55					
7	0.29	0.35	0.39	0.46	0.51	0.54				
8	0.27	0.33	0.36	0.43	0.48	0.50	0.52			
9	0.22	0.28	0.29	0.35	0.39	0.40	0.41	0.44		
10	0.23	0.30	0.33	0.42	0.49	0.54	0.57	0.59	0.49	

IMAGE 4 - EASTON METHOD

BAND	1	2	3	4	5	6	7	8	9	10
1										
2	0.84									
3	0.70	0.83								
4	0.57	0.68	0.74							
5	0.44	0.58	0.65	0.77						
6	0.34	0.48	0.57	0.70	0.78					
7	0.31	0.44	0.51	0.66	0.75	0.78				
8	0.28	0.42	0.49	0.64	0.73	0.78	0.79			
9	0.27	0.41	0.47	0.62	0.69	0.73	0.77	0.81		
10	0.14	0.24	0.30	0.44	0.52	0.58	0.62	0.66	0.65	

BAND	DESCRIPTION	
1	annulus 1	radius = 5- 10 pixels from center of FFT
2	annulus 2	radius = 10- 20 pixels from center of FFT
3	annulus 3	radius = 20- 35 pixels from center of FFT
4	annulus 4	radius = 35- 55 pixels from center of FFT
5	annulus 5	radius = 55- 80 pixels from center of FFT
6	annulus 6	radius = 80-110 pixels from center of FFT
7	annulus 7	radius = 110-145 pixels from center of FFT
8	annulus 8	radius = 145-195 pixels from center of FFT
9	annulus 9	radius = 195-255 pixels from center of FFT
10	original image 4	

CORRELATION COEFFICIENT MATRICES

IMAGE 9 - STROMBERG METHOD

BAND	1	2	3	4	5	6	7	8	9	10
1										
2	0.51									
3	0.39	0.62								
4	0.36	0.52	0.60							
5	0.31	0.46	0.53	0.60						
6	0.29	0.43	0.49	0.55	0.60					
7	0.27	0.40	0.46	0.54	0.57	0.61				
8	0.25	0.36	0.42	0.51	0.54	0.55	0.58			
9	0.21	0.30	0.34	0.41	0.44	0.45	0.46	0.49		
10	0.19	0.29	0.35	0.46	0.52	0.57	0.60	0.62	0.53	

IMAGE 9 - EASTON METHOD

BAND	1	2	3	4	5	6	7	8	9	10
1										
2	0.62									
3	0.54	0.80								
4	0.47	0.71	0.80							
5	0.41	0.63	0.70	0.79						
6	0.36	0.55	0.65	0.75	0.81					
7	0.32	0.51	0.60	0.72	0.79	0.83				
8	0.29	0.45	0.55	0.68	0.76	0.80	0.82			
9	0.28	0.43	0.52	0.64	0.73	0.78	0.79	0.83		
10	0.13	0.22	0.30	0.41	0.51	0.57	0.60	0.65	0.65	

BAND	DESCRIPTION
1	annulus 1 radius = 5- 10 pixels from center of FFT
2	annulus 2 radius = 10- 20 pixels from center of FFT
3	annulus 3 radius = 20- 35 pixels from center of FFT
4	annulus 4 radius = 35- 55 pixels from center of FFT
5	annulus 5 radius = 55- 80 pixels from center of FFT
6	annulus 6 radius = 80-110 pixels from center of FFT
7	annulus 7 radius = 110-145 pixels from center of FFT
8	annulus 8 radius = 145-195 pixels from center of FFT
9	annulus 9 radius = 195-255 pixels from center of FFT
10	original image 9

CORRELATION COEFFICIENT MATRICES

IMAGE 28 - STROMBERG METHOD

BAND	1	2	3	4	5	6	7	8	9	10
1										
2	0.44									
3	0.37	0.57								
4	0.30	0.49	0.56							
5	0.24	0.42	0.51	0.58						
6	0.22	0.40	0.49	0.56	0.58					
7	0.22	0.39	0.49	0.55	0.56	0.59				
8	0.19	0.35	0.45	0.51	0.53	0.54	0.55			
9	0.16	0.30	0.38	0.42	0.43	0.43	0.43	0.44		
10	0.19	0.35	0.45	0.52	0.55	0.58	0.59	0.60	0.49	

IMAGE 28 - EASTON METHOD

BAND	1	2	3	4	5	6	7	8	9	10
1										
2	0.62									
3	0.53	0.78								
4	0.43	0.67	0.77							
5	0.36	0.59	0.72	0.82						
6	0.32	0.54	0.67	0.78	0.82					
7	0.31	0.52	0.67	0.78	0.80	0.84				
8	0.28	0.49	0.64	0.75	0.79	0.81	0.82			
9	0.28	0.49	0.63	0.73	0.77	0.78	0.79	0.81		
10	0.20	0.36	0.47	0.57	0.61	0.64	0.65	0.67	0.67	

BAND	DESCRIPTION
1	annulus 1 radius = 5- 10 pixels from center of FFT
2	annulus 2 radius = 10- 20 pixels from center of FFT
3	annulus 3 radius = 20- 35 pixels from center of FFT
4	annulus 4 radius = 35- 55 pixels from center of FFT
5	annulus 5 radius = 55- 80 pixels from center of FFT
6	annulus 6 radius = 80-110 pixels from center of FFT
7	annulus 7 radius = 110-145 pixels from center of FFT
8	annulus 8 radius = 145-195 pixels from center of FFT
9	annulus 9 radius = 195-255 pixels from center of FFT
10	original image 28

CORRELATION COEFFICIENT MATRICES

IMAGE 29 - STROMBERG METHOD

BAND	1	2	3	4	5	6	7	8	9	10
1										
2	0.47									
3	0.33	0.39								
4	0.27	0.33	0.42							
5	0.28	0.34	0.41	0.45						
6	0.26	0.30	0.38	0.43	0.50					
7	0.25	0.29	0.36	0.42	0.46	0.49				
8	0.23	0.27	0.34	0.37	0.43	0.45	0.45			
9	0.19	0.22	0.25	0.28	0.32	0.33	0.34	0.35		
10	0.23	0.26	0.31	0.39	0.45	0.49	0.51	0.52	0.41	

IMAGE 29 - EASTON METHOD

BAND	1	2	3	4	5	6	7	8	9	10
1										
2	0.72									
3	0.59	0.60								
4	0.43	0.49	0.69							
5	0.43	0.50	0.64	0.71						
6	0.40	0.47	0.62	0.68	0.77					
7	0.37	0.44	0.59	0.66	0.73	0.75				
8	0.36	0.44	0.56	0.63	0.71	0.74	0.75			
9	0.34	0.42	0.53	0.60	0.66	0.69	0.71	0.73		
10	0.21	0.25	0.34	0.41	0.47	0.50	0.51	0.55	0.50	

BAND	DESCRIPTION
1	annulus 1 radius = 5- 10 pixels from center of FFT
2	annulus 2 radius = 10- 20 pixels from center of FFT
3	annulus 3 radius = 20- 35 pixels from center of FFT
4	annulus 4 radius = 35- 55 pixels from center of FFT
5	annulus 5 radius = 55- 80 pixels from center of FFT
6	annulus 6 radius = 80-110 pixels from center of FFT
7	annulus 7 radius = 110-145 pixels from center of FFT
8	annulus 8 radius = 145-195 pixels from center of FFT
9	annulus 9 radius = 195-255 pixels from center of FFT
10	original image 29

APPENDIX E

8-8-4 SAR DATA FORMAT

This appendix contains “Data Conversion Between ADT Image Formation Processor and VAX Computer”, ADT Project Memorandum No. 47PM-ADT-0053, 10 November 1986 by T. J. Morin.(Bessette *et al.*, 1991)

This document will describe the compressed data format that the Advanced Detection Technology (ADT) project has adopted as a standard for the turntable database and the subroutines that perform the conversion between the compressed format and the VAX format. The format, referred to as "8-8-4", allows a complex number to be represented with an 8-bit in-phase mantissa, an 8-bit quadrature mantissa and a common 4-bit exponent.

The decision to adopt the 8-8-4 format as the ADT standard was made for several reasons: The ADT Image Formation Processor (IFP) operates on data in this format, and compatibility between the turntable database data format and IFP images is desired. This format also provides for an efficient method for storing large amounts of calibrated radar data. The amount of space needed to store the data in 8-8-4 format (3 bytes per complex sample) is only 37% of the amount needed if it were stored in VAX format (COMPLEX*8).

A VAX complex number is represented as two normalized single precision floating point numbers whose bit layout is shown in figure 1. Each 4 byte number has an 8 bit excess 128 exponent in bits 7 to 14. Bit 15 is a sign bit, and bits 0 to 6 and 16 to 31 represent a normalized 24 bit fraction. Because a normalized number always has its most significant bit set, this is redundant and is therefore not represented. (See the VAX Architecture Handbook, chapter on Data Representation.)

The 8-8-4 format consists of two signed 8 bit I & Q mantissa fields and a common 4 bit exponent. The mantissa fields may or may not be normalized, so there is no implied most significant bit as in the VAX format. The bit layout of an 8-8-4 number is shown in Figure 1. The 8-8-4 I and Q values can be represented by the following equation:

$$V = (1/32) * (M/128) * (2 ** E)$$

$$\text{where} \quad \begin{array}{l} -128 \leq M \leq 127 \\ 0 \leq E \leq 15 \end{array}$$

The 8-8-4 format is intended to be used to store calibrated radar signal in meters (sqrt(RCS)). Because the bulk of the data values will fall between -10 meters and +10 meters (RCS of 0 - 100 sq. meters), we want to have as little loss of precision as possible for small data values. For this reason the additional 1/32 factor was added, ensuring acceptable granularity in the desired range and allowing a dynamic range of -1000 meters to +1000 meters. The 1/128 factor is inherent and results from representing the mantissas as 8-bit signed fractions. The lowest value that can be represented with full precision (a non-zero most significant bit) is 0.0156 meters, or -36.1 dBsm. Since the mantissas do not have to be normalized, however, representation of values down to -72 dBsm is possible. Table 1 shows the range of values that the 8-8-4 format is able to represent, and Figure 2 shows their distribution.

The algorithm which converts VAX to 8-8-4 format employs a lookup table. The low order 16 bits of a VAX word are mapped to a 4-bit exponent and 8-bit mantissa, and is done for both the I and Q words. The two exponents are compared and, if unequal, the mantissa with the smaller exponent is shifted right by the difference between the exponents. The exponent, I and Q mantissas are then packed into a three byte array element. The conversion is performed in place, with the 8-8-4 data replacing the VAX data in the array. Figure 3 details the format of the VAX and 8-8-4 data buffers.

The conversion from 8-8-4 to VAX format also makes use of a lookup table. For each of the I & Q values, the 4 bit exponent is placed into a register and shifted 8 bits left to make room for the mantissa. The mantissa is placed in the low eight bits of the register and the resultant 12-bit value is used as an offset into a table of floating point values. The process starts at the end of the complex array and works backwards in order to facilitate an "in place" conversion, so the output VAX data replaces the input 8-8-4 data in the buffer. The macro source for both conversion routines is included in the appendix.

The VAX to 8-8-4 lookup table contains 2^{16} values. Although there are only 4096 distinct values, this allows for fast translation of a floating point number to a packed value by using the low order 16 bits of the number as an offset into the table. The table is constructed by taking all combinations of 16 bits and treating them as the low order bits of a floating point number. The most significant bits are extracted, the implied bit is set, the excess (128) is removed from the exponent and the new bias (1/32) is inserted, and the sign bit is set if necessary. The original 16 bit number is then used as the address in the table.

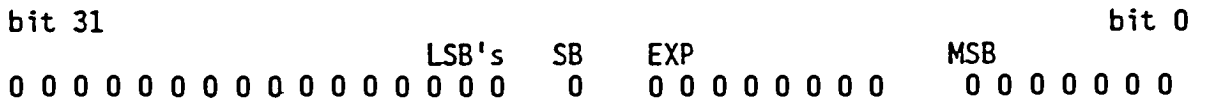
The 8-8-4 to VAX table is similarly constructed, using all combinations of 12 bit values (i.e., 4096 values). Source code for both table construction routines is appended.

A timing analysis was done in batch mode for four cases of access modes and one case to determine the overhead involved in executing a batch job. The five cases, denoted as cases A - E, all consisted of 15 separate batch jobs. In cases A - D, complex samples were either read from magnetic disk or written to magnetic disk. Each experiment involved approximately one million complex samples. Case E consisted simply of the batch execution of a "no-op" job to determine what overhead (CPU and elapsed time) is involved in executing in the batch mode. All jobs ran on an unloaded machine. The five cases are described below:

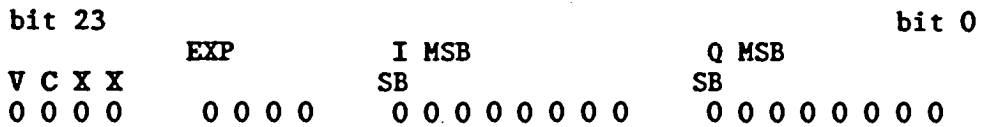
- Case A: VAX complex samples are converted to "8-8-4" format and written to magnetic disk.
- Case B: The same complex samples generated in Case A are read from magnetic disk and converted to VAX complex*8.
- Case C: VAX complex samples are written to magnetic disk.
- Case D: The same samples generated in Case C are read from magnetic disk.
- Case E: Overhead case. A job which does nothing is submitted in batch mode.

Table 2 summarizes the timing results in units of CPU and elapsed seconds per sample in terms of how long it takes to read/write complex data. The table indicates that, although more CPU time is needed to convert the data to and from 8-8-4 format, the elapsed time involved in accessing the 8-8-4 data is less than the time involved in accessing VAX complex floating point data. For example, a typical operation reading 8-8-4 data from a disk runs 23% faster, consumes 63% less space and takes only 5 microseconds more CPU time per sample.

VAX Single Precision Floating Point Bit Layout



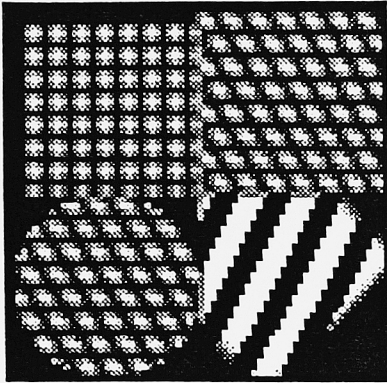
8-8-4 Complex Format



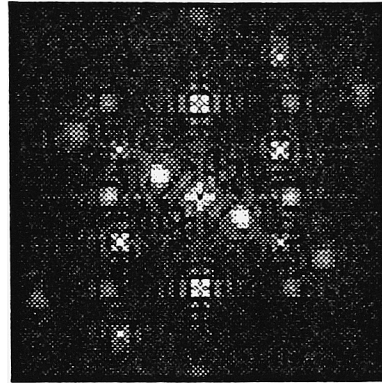
- Where:
- LSB = Least Significant Bit
 - MSB = Most Significant Bit
 - SB = Sign Bit
 - EXP = Exponent
 - V = Valid data bit
 - C = Control bit (0=data word,1=header word)
 - X = Not used

APPENDIX F

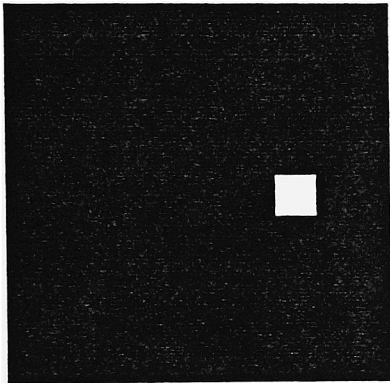
(a) $f[x,y]$



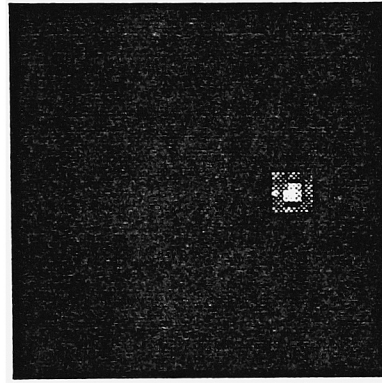
(b) $|F[\xi,\eta]|$



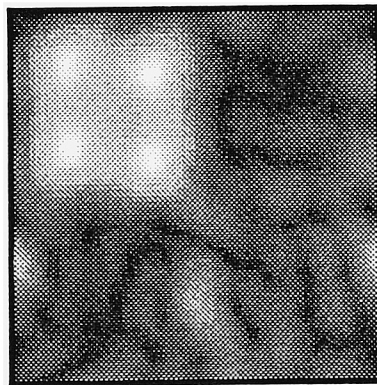
(c) $A_1[\xi,\eta]$



(d) $|F[\xi,\eta] \cdot A_1[\xi,\eta]|$



(e) $|\mathcal{F}^{-1}\{F[\xi_0,\eta] \cdot A_1[\xi_0,\eta]\}|$



TEXTURE ANALYSIS USING EASTON'S METHOD WITHOUT CENTERING